

Biofunctional Nanodot Arrays in Living Cells Uncover Synergistic Co-Condensation of Wnt Signalodroplets

Michael Philippi, Christian P. Richter, Marie Kappen, Isabelle Watrinet, Yi Miao, Mercedes Runge, Lara Jorde, Sergej Korneev, Michael Holtmannspötter, Rainer Kurre, Joost C. M. Holthuis, K. Christopher Garcia, Andreas Plückthun, Martin Steinhart,* Jacob Piehler,* and Changjiang You*

Qualitative and quantitative analysis of transient signaling platforms in the plasma membrane has remained a key experimental challenge. Here, biofunctional nanodot arrays (bNDAs) are developed to spatially control dimerization and clustering of cell surface receptors at the nanoscale. High-contrast bNDAs with spot diameters of ≈ 300 nm are obtained by capillary nanostamping of bovine serum albumin bioconjugates, which are subsequently biofunctionalized by reaction with tandem anti-green fluorescence protein (GFP) clamp fusions. Spatially controlled assembly of active Wnt signalosomes is achieved at the nanoscale in the plasma membrane of live cells by capturing the co-receptor Lrp6 into bNDAs via an extracellular GFP tag. Strikingly, co-recruitment is observed of co-receptor Frizzled-8 as well as the cytosolic scaffold proteins Axin-1 and Disheveled-2 into Lrp6 nanodots in the absence of ligand. Density variation and the high dynamics of effector proteins uncover highly cooperative liquid–liquid phase separation (LLPS)-driven assembly of Wnt “signalodroplets” at the plasma membrane, pinpointing the synergistic effects of LLPS for Wnt signaling amplification. These insights highlight the potential of bNDAs for systematically interrogating nanoscale signaling platforms and condensation at the plasma membrane of live cells.

meshwork and segregation by protein–lipid interactions in conjunction with phase transitions of proteins and lipids.^[1–5] The resulting hierarchical compartmentalization in the plasma membrane in turn regulates the functional organization of signaling complexes,^[6–9] in particular by promoting dynamic receptor clustering, which has emerged as a key principle for amplifying downstream signaling.^[10–14] The molecular and cellular mechanisms responsible for receptor clustering, however, have remained largely unresolved.^[11] Recently, liquid–liquid phase separation (LLPS) of proteins induced by multivalent protein–protein interactions emerged as a key principle driving dynamic receptor clustering.^[15–21] Experimentally pinpointing and characterizing the involvement of LLPS in the formation and activation of signaling complexes in the plasma membrane has remained challenging due to the nanoscale dimensions and the high dynamics of such entities.

Here, we introduce biofunctional nanodot array (bNDA) technology as a generic approach to assemble signaling platforms with well-defined geometry in the plasma membrane of live cells. To this end, we employed capillary nanostamping^[22,23] for printing functionalized bovine serum albumin (BSA) onto

1. Introduction

The plasma membrane of mammalian cells is dynamically compartmentalized at the micro- and nanoscale, caused by an intricate interplay of corral formation by the cortical actin

M. Philippi, C. P. Richter, M. Kappen, I. Watrinet, M. Runge, L. Jorde, S. Korneev, M. Holtmannspötter, R. Kurre, J. C. M. Holthuis, M. Steinhart, J. Piehler, C. You
Department of Biology/Chemistry and Center for Cellular Nanoanalytics (CellNanOs)
Osnabrück University
49076 Osnabrück, Germany
E-mail: martin.steinhart@uos.de; piehler@uos.de;
cyou@uni-osnabrueck.de

Y. Miao, K. C. Garcia
Department of Molecular and Cellular Physiology
Department of Structural Biology
Howard Hughes Medical Institute
Stanford University School of Medicine
Stanford, CA 94305, USA
A. Plückthun
Department of Biochemistry
University of Zurich
Winterthurerstr. 190, Zurich 8057, Switzerland



The ORCID identification number(s) for the author(s) of this article can be found under <https://doi.org/10.1002/smll.202203723>.

© 2022 The Authors. Small published by Wiley-VCH GmbH. This is an open access article under the terms of the Creative Commons Attribution License, which permits use, distribution and reproduction in any medium, provided the original work is properly cited.

DOI: 10.1002/smll.202203723

hydrophobic glass coverslips, yielding nanodots with < 300 nm diameter. By subsequent conjugation with an engineered GFP binder, efficient, high-density capturing of GFP-tagged proteins was achieved, yielding very high contrast in vitro and in live cells. For proof-of-concept experiments, we employed bNDAs to assemble functional Wnt signalosomes^[24] that have recently been proposed to involve LLPS.^[25,26] The canonical Wnt signaling pathway activates the transcription factor β -catenin, which is an evolutionally highly conserved regulator of stem cell fate decision.^[27–29] Wnt signalosome formation is initiated by crosslinking of low-density lipoprotein receptor-related protein 5/6 (Lrp5/6) and the co-receptor Frizzled (Fzd) in the plasma membrane via the Wnt ligand^[30] (Figure 1A). Receptor heterodimerization initiates recruitment of the cytosolic scaffold proteins Axin and Disheveled (Dvl), leading to the formation of multiprotein assemblies in the plasma membrane, the so-called Wnt signalosomes.^[24,31]

The molecular mechanisms underlying Wnt signalosome formation, however, are currently under debate. Interestingly, not only ligand-induced heterodimerization and/or hetero-oligomerization of Fzd and Lrp6 can initiate signalosome

formation and β -catenin activation,^[32–37] but also homo-oligomerization of Lrp6,^[38,39] with its intracellular multiple binding motifs that interact with Axin1 playing a critical role.^[40,41] These observations could be explained by LLPS being a driving force to form Wnt signalosome as condensates,^[25,26] and indeed, co-condensates of the cytosolic scaffold proteins Axin and Disheveled (Dvl) have been observed.^[42–44] However, systematic analyses of Wnt signalosome assembly and dynamics in the plasma membrane under well-defined conditions have been lacking so far.

Here, we applied bNDAs for spatially controlling Wnt signalosome assembly in plasma membrane of live cells (Figure 1B). Strikingly, dimerizing and clustering of Lrp6 in bNDAs promoted ligand-independent recruitment of the co-receptor Fzd8 and the cytosolic effector proteins Axin1 and Dvl2 as well as activation of downstream signaling. Quantitative analysis at single nanodot level revealed dynamic, highly cooperative effector binding and a critical role of Lrp6 density. Our insights strongly support that Wnt signalosome assembly is driven by co-condensation of Axin and Dvl, which is regulated by local enrichment of Axin upon transient interaction with clustered Lrp6.

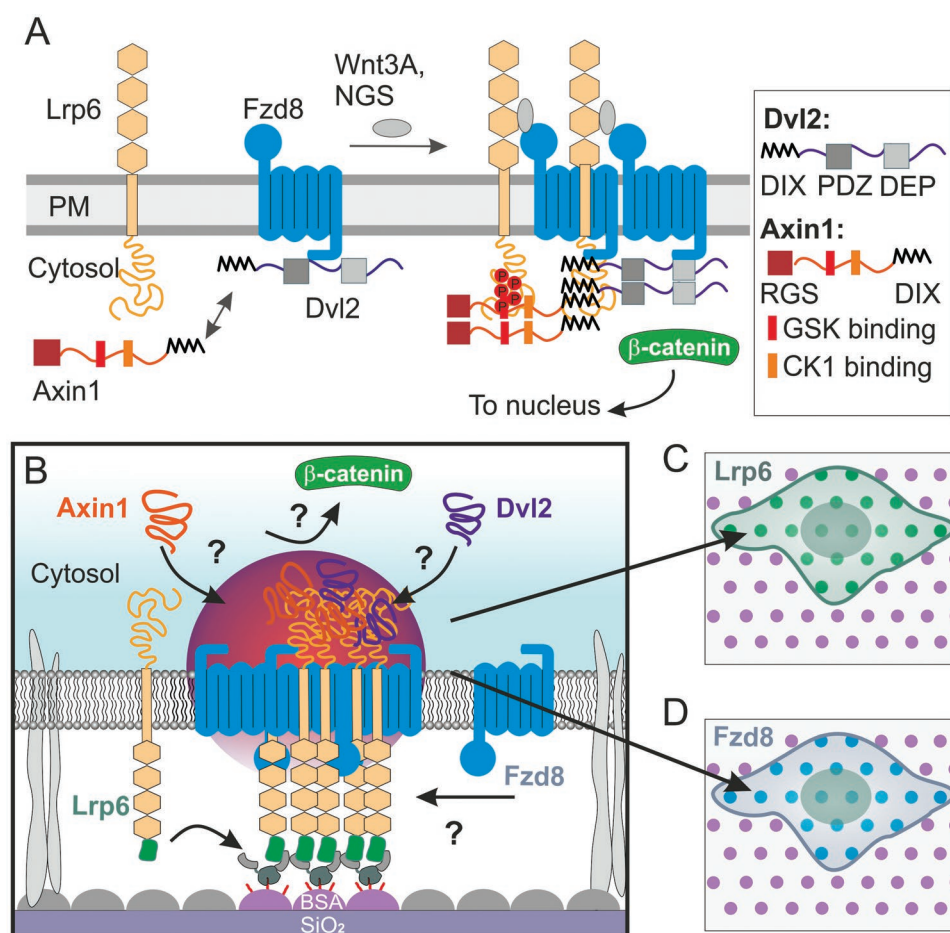


Figure 1. Reorganization of the Wnt signalingrelevant proteins in live cell plasma membrane by nanodot arrays (NDAs). A) Scheme summarizing the current view of Wnt signalosome formation responsible for activating the Wnt/ β -catenin pathway. The intrinsically disordered scaffold proteins Dvl2 and Axin1 and their binding motifs are outlined in the box. B) Concept of live cell protein nanodot arrays for inducing Wnt signalosome assembly by locally clustering Lrp6 in the plasma membrane via an extracellular GFP-tag. C,D) Potential recruitment of Wnt signaling proteins labeled Fzd8, Axin1 and Dvl2 into Lrp6 bNDAs can be detected and quantified by total internal reflection fluorescence (TIRF) microscopy.

2. Results

2.1. Protein-Based Surface Functionalization for Contact Lithography with Nanoscale Resolution

To achieve efficient, high-density surface biofunctionalization and high precision capillary nanostamping, we applied BSA as an ink, which has proven well compatible with high-contrast contact lithography via physisorption onto hydrophilic and hydrophobic surfaces.^[45,46] For subsequent functionalization, BSA was conjugated with amine-functionalized HaloTag ligand (HTL)^[47] using amide coupling chemistry. The synthesized ^{HTL}BSA had an average degree of functionalization of ≈ 13 HTL

moieties per BSA according to mass spectrometry and was used for bioorthogonal covalent capturing of target proteins fused to the HaloTag^[47] as depicted in **Figure 2A**. To promote adsorption rates of BSA to glass surfaces and to minimize spreading of the printed solution, the glass substrates were rendered hydrophobic by silanization. Surface modification with 1-naphthylmethyltrichlorosilane (NMTS) turned out most efficient compared to other hydrophobic silanes (Figure S1A, Supporting Information), for which the binding kinetics of BSA was quantified by label-free detection based on reflectance interference (RIF) under flow-through conditions.^[48–50] Very rapid and stable BSA coating was observed on NMTS-treated silica substrates (Figure 2B; Figure S1b, Supporting Information) with the final

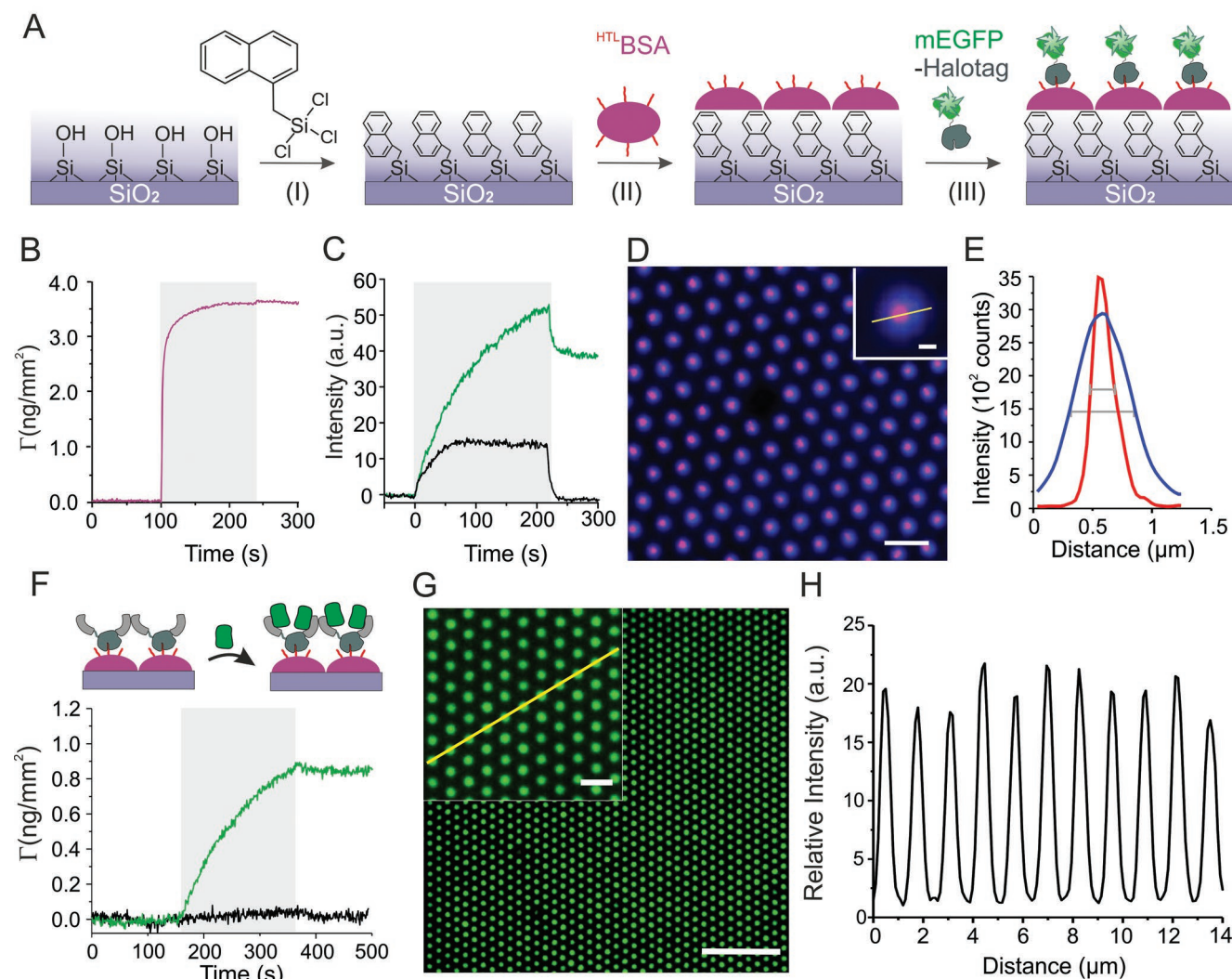


Figure 2. Surface functionalization for fabricating high-contrast bNDA on glass support. A) Scheme of the procedure: silanization by 1-naphthylmethyltrichlorosilane (NMTS) for rendering the surface hydrophobic (I), binding of HaloTag Ligand-BSA conjugate (^{HTL}BSA) to NMTS-coated substrates (II), and specific biofunctionalization with HaloTag-mEGFP (III). B) Real-time kinetics of 10 μ M ^{HTL}BSA binding onto a NMTS-coated silica surface monitored by label-free RIF detection. C) Fluorescence signal during injection of 2 μ M HaloTag-mEGFP binding to a ^{HTL}BSA-coated substrate (green) as detected by TIRFS. Only the background signal was detected upon injection of 2 μ M mEGFP without HaloTag on the same surface (black). D) Merged dSTORM image (red) and diffraction limited, unprocessed TIRF image (blue) of ^{AT647N}BSA printed into a bNDA. Scale bar: 1 μ m (inset: 100 nm). E) Intensity profiles across the line shown in panel (D). The diameters of nanodots were obtained as the FWHM of the intensity profile. F) mEGFP binding after functionalization of ^{HTL}BSA-coated surface with tdClamp-HaloTag as detected by RIF. G) Deconvolved TIRF microscopy image of mEGFP bound to tdClamp-functionalized bNDA. Scale bar: 10 μ m, inset: 2 μ m. H) Relative intensity profile highlighted by the yellow line shown in the inset of panel (G).

mass signal of $\approx 3.5 \text{ ng mm}^{-2}$ being in good agreement with formation of a BSA monolayer.^[51] Specific immobilization of the mEGFP-HaloTag fusion protein on the ^{HTL}BSA-coated surface was confirmed by real-time total internal reflection fluorescence (TIRF) detection (Figure 2C), with an association rate constant (k_{on}) of $\approx 10^3 \text{ M}^{-1} \text{ s}^{-1}$ (Table S1, Supporting Information) in line with previous kinetics studies of the HaloTag-HTL interaction.^[52]

To explore the capability of generating high-contrast biofunctional nanodot arrays (bNDAs), BSA labeled with ATTO647N (^{AT647N}BSA) was stamped onto NMTS-treated glass microscopy coverslips using an established protocol.^[22] Because the dot sizes and distance are close to the diffraction limit (Figure S1C, Supporting Information), we applied image deconvolution for more reliable image analysis,^[22] which not only increased the resolution, but also the contrast (Figure S1D, Supporting Information). To more precisely quantify the diameter of the nanodots, we resolved the spatial distribution of printed BSA in nanodots beyond the diffraction limit by direct stochastic optical reconstruction microscopy (dSTORM) of the printed ^{AT647N}BSA bNDAs (Figure 2D,E; Figure S1E, Supporting Information). The dSTORM super-resolution images revealed an average diameter of $256 \pm 33 \text{ nm}$ ($N = 10$) for the nanodots, which is substantially below the $450 \pm 68 \text{ nm}$ ($N = 11$) observed for deconvolved TIRFM images. The contrast of bNDA was calculated as the central intensity of a nanodot divided by the intensity baseline between nanodots. In line with the increased resolution, the dSTORM images moreover revealed the highest contrast achieved by BSA capillary nanoprinting as the consequence of background-free imaging between the nanodots (Figure S1H, Supporting Information).

2.2. Efficient Capturing of GFP-Tagged Proteins into bNDAs

Staining of ^{HTL}BSA bNDAs with HaloTag-mEGFP yielded a good contrast of 10 ± 2.6 ($N = 15$), but the intensities of the dots within the nanopatterns showed a rather heterogeneous distribution (Figure S2A–C, Supporting Information). Similarly, direct capturing of GFP-tagged receptors, also carrying a HaloTag, in the plasma membrane of live cells lacked efficiency and homogeneity, yielding a contrast below 10 (Figure S2D–F, Supporting Information). Ascribing this performance to the relatively slow reaction of the HaloTag with ^{HTL}BSA (cf. Figure 2C; Table S1, Supporting Information), we turned to a robust, high-affinity GFP binder, the so-called “GFP-clamp” engineered from DARPins^[53] for capturing GFP-tagged proteins into bNDAs. To furthermore promote dimerization of captured receptors at molecular scale, which has been implicated in the activation of Wnt receptors,^[35,36] we fused two copies of the GFP-clamp via a linker that included a HaloTag (tdClamp-HaloTag) for in situ coupling to immobilized ^{HTL}BSA. Rapid and specific binding of mEGFP to ^{HTL}BSA-coated surfaces functionalized with tdClamp-HaloTag was confirmed by reflectance interference detection (Figure 2F) yielding a 25-fold higher k_{on} than found for direct binding of HaloTag to ^{HTL}BSA (Table S1, Supporting Information). From the signal amplitude, 1/3 of a protein monolayer was estimated to have formed, which corresponds to a binding capacity of $\approx 13000 \text{ GFP molecules } \mu\text{m}^{-2}$. As a

result of this improved capturing strategy, binding of 200 nm mEGFP to ^{HTL}BSA bNDAs pretreated with tdClamp-HaloTag robustly yielded a strikingly high contrast of 19.4 ± 1.9 ($N = 9$) (Figure 2G,H), providing ideal conditions for receptor clustering in live cells.

2.3. Efficient Reorganization of Lrp6 in the Plasma Membrane Induces Active Wnt Signalosomes

We employed tdClamp-functionalized bNDAs for exploring whether Wnt signalosome assembly could be triggered by clustering Lrp6 as depicted in Figure 3A. To this end, HeLa cells co-expressing Lrp6 fused to an N-terminal mEGFP-tag and Frizzled 8 fused to the SNAP-tag (SNAP-Fzd8) labeled with Dy647 were cultured on tdClamp-functionalized bNDAs. Strong enrichment of mEGFP-Lrp6 within nanodots was observed, corroborating that highly efficient and selective immobilization of transmembrane receptor was induced (Figure 3B). Strikingly, significant co-clustering of Fzd8 in bNDAs was observed (Figure 3B; Figure S2J–L, Supporting Information), which was strongly dependent on the Lrp6 density (Figure 3C–E). These experiments highlighted that Fzd8 can interact with clustered Lrp6 in the absence of a heterodimerizing agonist such as Wnt in an Lrp6 density-dependent manner. By the contrast, clustering of mEGFP-fused Fzd8 in bNDAs did not recruit Lrp6 (Figure S2M–O, Supporting Information), indicating that Lrp6 bNDAs have more potential to activate Wnt signaling than Fzd8 bNDAs.

Since oligomerization of Lrp6 has previously been shown to activate Wnt/ β -catenin signaling,^[38,39] we speculated that the high-density Lrp6 bNDAs are capable to assemble active signalosomes. To verify Wnt signaling at the single cell level, we quantified the β -catenin density in the nucleus by immunofluorescence (IF) staining (Figure 3F). For HeLa cells expressing mEGFP-Lrp6 alone cultured on bNDAs, no difference of β -catenin as compared to the basal level in unpatterned, untransfected HeLa was observed (Figure 3G). However, HeLa cells co-expressing mEGFP-Lrp6 and SNAP-Fzd8 showed \approx twofold increased β -catenin level in the nucleus upon Lrp6 nanoclustering in bNDAs (Figure 3G), in good agreement with agonist-activated Wnt signaling.^[32] By contrast, bNDAs of Lrp6 lacking its intracellular domain (Lrp6 Δ ICD) did not increase the β -catenin level even in the presence of co-expressed Fzd8 (Figure 3G), in line with the important tandem PPP(S/T)P motifs located in the Lrp6 ICD being critical for Wnt/ β -catenin signaling.^[38,54] As a positive control, unpatterned HeLa cells were treated overnight with $1 \mu\text{M}$ of the glycogen synthase kinase 3 (GSK3) inhibitor BIO (6-bromindirubin-3-oxime) to prevent phosphorylation of β -catenin and the subsequent degradation. IF resulted in a 2.3 ± 0.9 fold ($N = 24$) increase in the nucleus compared to the basal level (Figure 3H). A further increase of 3.8 ± 1.6 fold ($N = 23$) was observed for HeLa cells stimulated with the potent next generation surrogate (NGS) Wnt^[34] (Figure 3H). Together, these results confirm that co-clustering of Lrp6 and Fzd8 in nanodot arrays lead to spatially controlled Wnt signalosomes in live cells. Wnt signalosome downstream signaling is mediated by the recruitment of the cytosolic effector proteins Axin and Dvl.^[55]

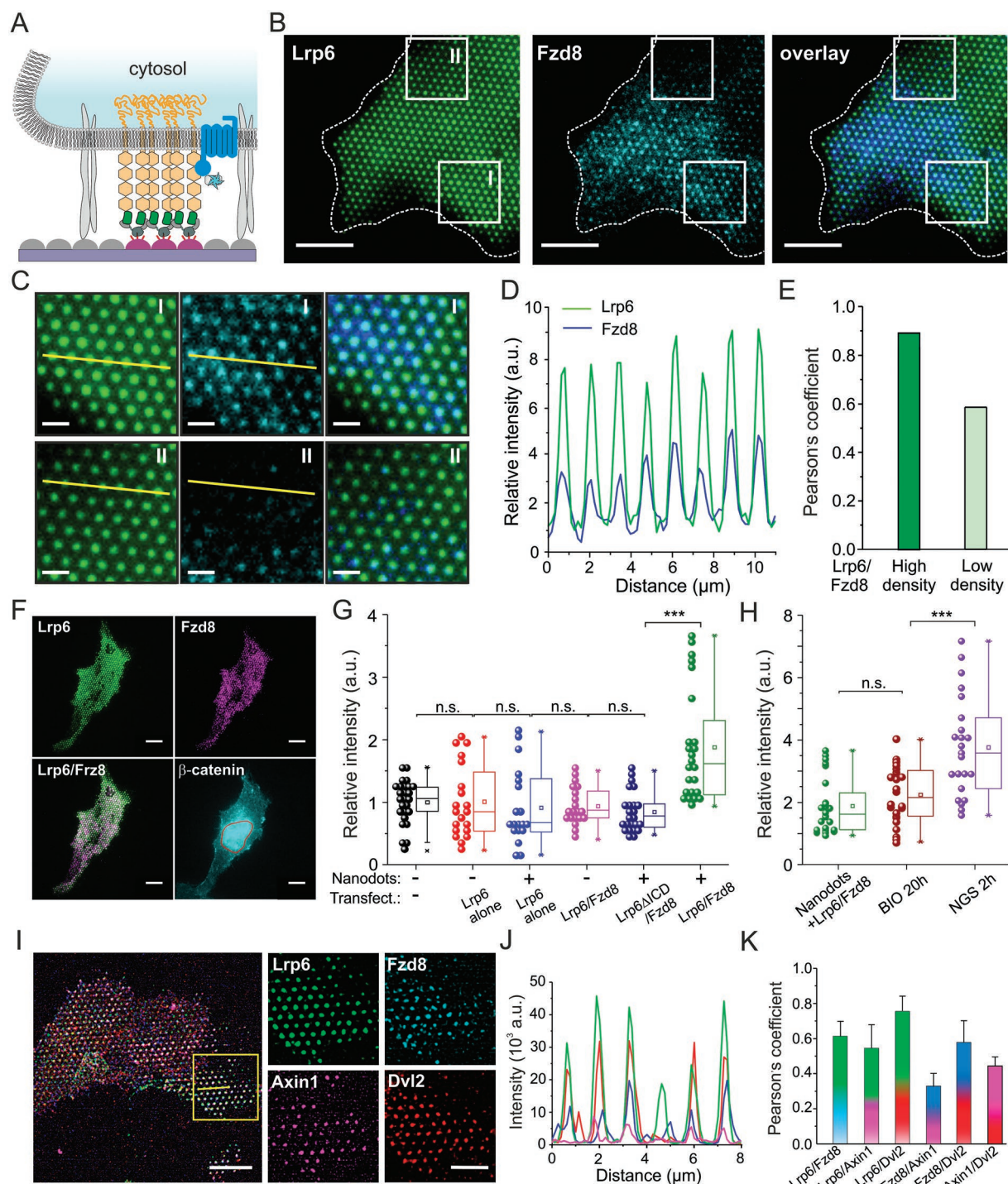


Figure 3. Assembly of functional Wnt signalosomes upon clustering Lrp6 into bNDAs. **A)** Scheme illustrating the enrichment of Lrp6 into bNDA via an N-terminal mEGFP-tag. Signalosome assembly was probed by co-expression of Fzd8 fused to an N-terminal SNAP-tag labeled with Dy647. **B)** Representative TIRF microscopy image of a live HeLa cell co-expressing mEGFP-Lrp6 (green) and DY647-SNAP-Fzd8 (cyan) cultured on bNDA. Scale bars: 10 μm. **C)** Zoom into regions with higher (I) and lower (II) density of captured Lrp6. Scale bars: 2 μm. **D)** Relative intensity profile marked in panel C region I. **E)** Pearson's correlation coefficient of the marked regions I and II. **F)** Representative TIRF microscopy images of a fixed HeLa cell expressing mEGFP-Lrp6 (green) and SNAP-Fzd8 labeled with Dy549 (magenta) captured into an bNDA. After fixation, β-catenin was stained by immunofluorescence and imaged by epifluorescence microscopy (cyan). Scale bars: 10 μm. **G,H)** β-catenin levels in the nucleus of HeLa cells cultured under different conditions quantified by IF in individual cells. Statistics by t-test. *p*-value > 0.05 for non-significant (n.s.). *p* < 0.001 for ***. **I–K)** Four-color TIRF microscopy imaging of cytosolic effector proteins Axin1 and Dvl1 in Wnt signalosomes. **I)** Representative TIRF image of HeLa cell co-expressing mEGFP-Lrp6 (green), SNAP-Fzd8 (magenta), mTagBFP-Axin1 (blue) and Dvl2-td-mCherry (red). Overview images with all four colors overlaid (left) and a zoomed region show all four channels. Scale bars: 10 μm (left), 5 μm (zoomed images). **J)** Intensity profile of highlighted line profile in panel I. **K)** Co-localization analysis for all channels.

Having observed activation of canonical Wnt signaling upon Lrp6 clustering into bNDAs, we therefore also probed co-clustering of Axin1 and Dvl2 in bNDAs. Using four-color TIRF microscopy, strong enrichment of Axin1 and Dvl2 at Lrp6/Fzd8 signalodots could be observed (Figure 3I–K), corroborating successful assembly of comprehensive and fully functional Wnt signalosomes into bNDAs (termed “Wnt signalodots” in the following).

2.4. Wnt Signalosome Formation is Driven by Cytosolic Effector Proteins

Exploiting the highly controlled assembly of Wnt signalodots, we interrogated the mechanistic principles driving Wnt signalosome formation in more detail. In particular, we were interested in quantifying the interaction and dynamics of Axin1 and Dvl2, respectively. Culturing HeLa cells co-expressing mEGFP-Lrp6, SNAP-Fzd8 and a tandem mCherry-Axin1 fusion (tdmCherry-Axin1) on tdClamp-functionalized bNDAs yielded high co-localization of all three proteins (Figure 4A–D; Figure S3A, Supporting Information). This observation is in line with previous reports that Axin1—the core component of the β -catenin destruction complex—is recruited to the plasma membrane during canonical Wnt signaling.^[54–56] Efficient recruitment of Axin1 to Lrp6 nanodots could be explained by direct interactions of Axin1 with Lrp6 via the tandem PPP(S/T)P motifs of Lrp6 located in its ICD.^[54,55] In line with this hypothesis, bNDAs formed from Lrp6 lacking the intracellular domain (Lrp6 Δ ICD) did not recruit Axin1 (Figure 4E–H; Figure S3B, Supporting Information). Interestingly, Fzd8 was not enriched in Lrp6 Δ ICD bNDAs either, suggesting that the intracellular domain of Lrp6 and its interaction with Axin1 plays a key role in Wnt-independent receptor interactions. Similarly, Dvl2 was strongly enriched in Lrp6 bNDAs for experiments carried out in wt HeLa cells that express endogenous Axin1/2 (Figure 4I–L; Figure S3C, Supporting Information). By contrast, much lower binding of Dvl2 was found for the same experiment carried out in genome engineered HeLa cell line that lacks all Axin variants (HeLa Axin1/2 DKO) (Figure 4M–P, Figure S3D, Supporting Information). Strikingly, recruitment of Fzd8 into Lrp6-bNDAs was also substantially diminished under these conditions, corroborating that Axin is involved in mediating co-clustering of the receptor subunits. Moreover, reduced density of Lrp6 was found in these experiments, highlighting the cooperation of receptor and effector interactions in the Wnt signalosome assembly.

To pinpoint this feature, we correlated fluorescence intensities of Lrp6 with Axin1 and Fzd8, respectively, in each signalodot. To account for inhomogeneous illumination, the contrasts in each channel were calculated by comparing the intensity of individual dot to its local background. A logarithmic correlation based on ≈ 700 signalodots confirmed that Axin1 recruitment depends on Lrp6 density in a biphasic mode (Figure 4Q): At an Lrp6 contrast below 10, Axin1 recruitment remained negligible (contrast <2). At Lrp6 density above this threshold, however, recruitment of Axin1 strongly increased, reaching a contrast above 10. Recruitment of Fzd8 showed a very similar biphasic dependence on Lrp6 density though with somewhat lower

slope of the correlation above the threshold of 10 (Figure 4R). These biphasic dependence of Lrp6 density supports high cooperativity of receptor and effector interactions, in line with the hypothesis that signalosome formation is being triggered by co-condensation of receptor and effector proteins. Interestingly, biphasic dependence could be observed for neither Dvl2 nor Fzd8 without overexpressing Axin1 (Figure 4S,T), highlighting the critical role of Axin1 in this process.

2.5. Effector Protein Dynamics Supports LLPS-Driven Signalodot Assembly

Speculating that liquid–liquid phase separation (LLPS) is an important driving force for signalosome formation, we explored the dynamics of Axin1 in signalodot arrays. One hallmark of protein condensates is a rapid exchange with the environment due to transient multivalent interactions.^[57] We therefore quantified by fluorescence recovery after photobleaching (FRAP) the exchange kinetics at the level of individual signalodots in HeLa cells expressing mEGFP-Lrp6, SNAP-Fzd8 labeled with Dy647 and tdmCherry-Axin1. Strikingly, rapid recovery was observed for Axin1, but not Lrp6 and Fzd8 (Figure 5A,B; Figure S4A and Video S1, Supporting Information). An average calculated from 30 individual signalodots yielded an overall 34% recovery within 200 s observation time. Likewise, FRAP experiments with HeLa cells expressing mEGFP-Lrp6, SNAP-Fzd8 labeled with Dy647 and Dvl2-tdmCherry revealed dynamic exchange of Dvl2 at the single signalodot level (Figure 5C,D; Figure S4B and Video S2, Supporting Information).

As the rapid exchange dynamics are in line with LLPS of Axin1 and Dvl2 in Wnt signalodots, we performed similar FRAP experiments with Axin1/Dvl2 co-condensates that spontaneously formed upon overexpression HaloTag-Axin1 labeled with silicon rhodamine (SiR) and Dvl2-mCherry, respectively, in the cytosol of HeLa cells (Figure 5E; Video S3, Supporting Information). In line with previous observations,^[42,44] co-condensates of Axin1 and Dvl2 showed rapid exchange dynamics yielding similar recovery characteristics as in signalodot arrays (Figure 5F). Dvl2 droplet formation was largely independent of Axin1 expression, but the concentration of Dvl2 in condensates negatively correlated with the Axin1 expression levels (Figure 5G). The fluidity of droplets was moreover confirmed by sub-droplet FRAP and by observing fusion and fission (Figure S4D,E and Videos S4 and S5, Supporting Information). Single-molecule tracking analysis of sub-stoichiometrically labeled Dvl2-HaloTag revealed high mobility inside the droplets with a heterogeneity of the diffusion properties, suggesting different types of interactions (Figure 5H,I; Video S6, Supporting Information). Similar condensation properties were observed for purified Dvl2 recombinantly produced in *E. coli* (Figure S4F–H, Supporting Information).

2.6. Axin1/Dvl2 Nanodroplets at the Membrane do not Trigger Signalosome Assembly

We therefore hypothesized that Wnt signalosome formation at the plasma membrane is driven by co-condensation of

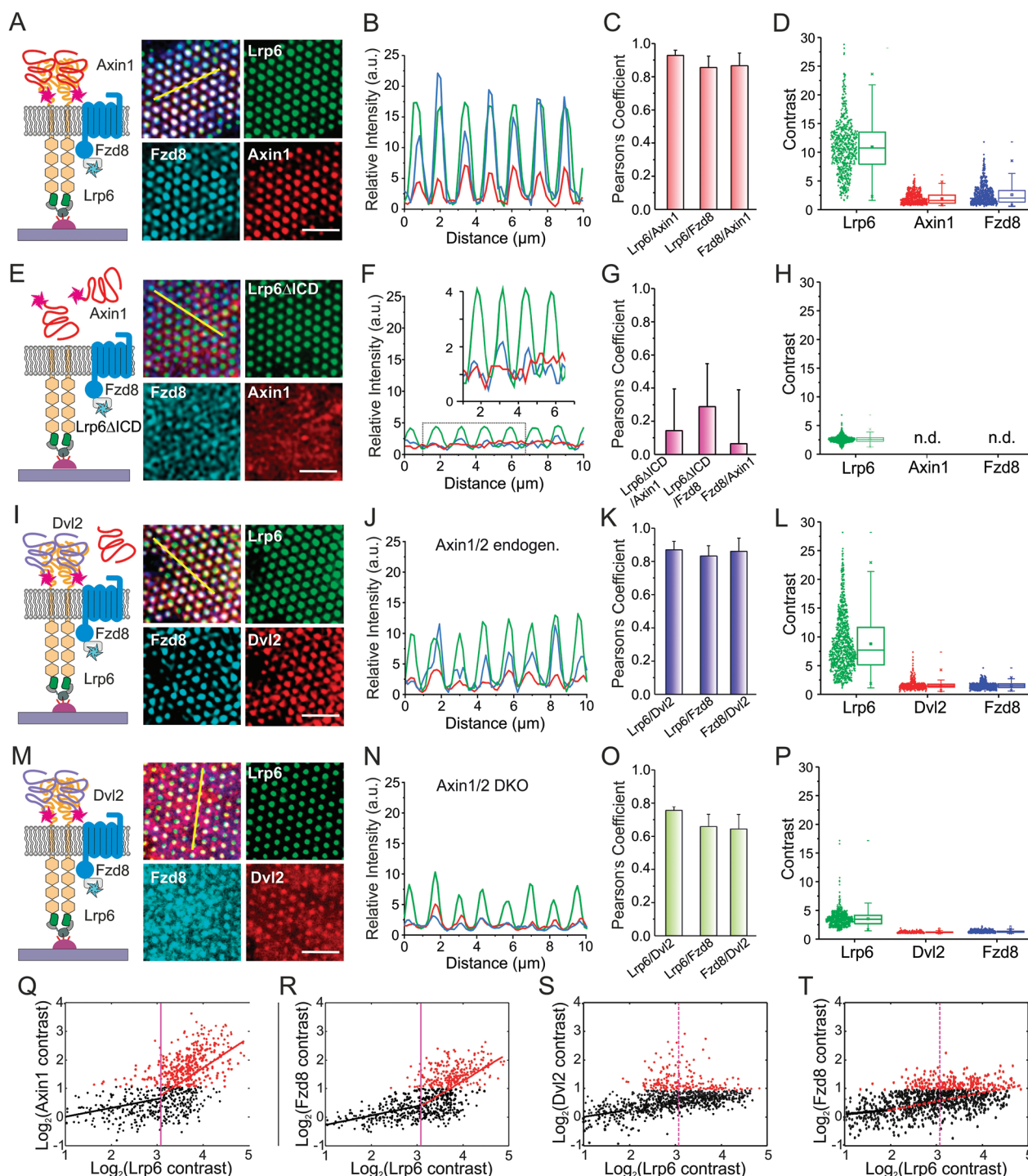


Figure 4. Co-operative recruitment of receptors and effectors into Wnt signalodots. A–D) Co-recruitment of Axin1 and Fzd8 into Lrp6 bNDAs. A) Deconvolved 3-color TIRF microscopy images of a HeLa cell co-expressing mEGFP-Lrp6 (green), SNAP-Fzd8 labeled with Dy647 (blue) and tdmCherry-Axin1 (red). B) Intensity profile highlighted by the yellow line in panel A. C) Pearson's correlation analysis with mean \pm s.d. obtained from 9 line profiles in 3 cells. D) Single nanodot intensity analysis for all three channels. E–H) Control experiment with Lrp6 lacking its intracellular domain. E) Deconvolved TIRF microscopy images of a HeLa cell co-expressing mEGFP-Lrp6 Δ ICD (green), SNAP-Fzd8 labeled with Dy647 (blue) and tdmCherry-Axin1 (red). F) Intensity profile highlighted by the yellow line in panel (E). G) Pearson's correlation analysis with mean \pm s.d. obtained from 7 cells. H) Single nanodot intensity analysis for all three channels. I–L) Co-recruitment of Dvl2 and Fzd8 into Lrp6 bNDAs. I) Deconvolved 3-color TIRF microscopy images of a HeLa cell co-expressing mEGFP-Lrp6 (green), SNAP-Fzd8 labeled with Dy647 (blue) and Dvl2-tdmCherry (red). J) Intensity profile highlighted by the yellow line in panel (I). K) Pearson's correlation analysis with mean \pm s.d. obtained from 9 line profiles in 3 cells. L) Single nanodot intensity analysis for all three channels. M–P) Same experiment as shown in panels (I–L), but carried out in HeLa cells lacking Axin1 and Axin2 (Axin1/2 DKO). Scale bars: 5 μ m for all images. Q,R) Single nanodot intensity correlation analysis for Q) Lrp6 and Axin1 and for R) Lrp6 and Fzd8 from the experiment shown in panel (A). Single nanodot intensity correlation analysis for S) Lrp6 and Dvl2 and for T) Lrp6 and Fzd8 from the experiment shown in panel (I).

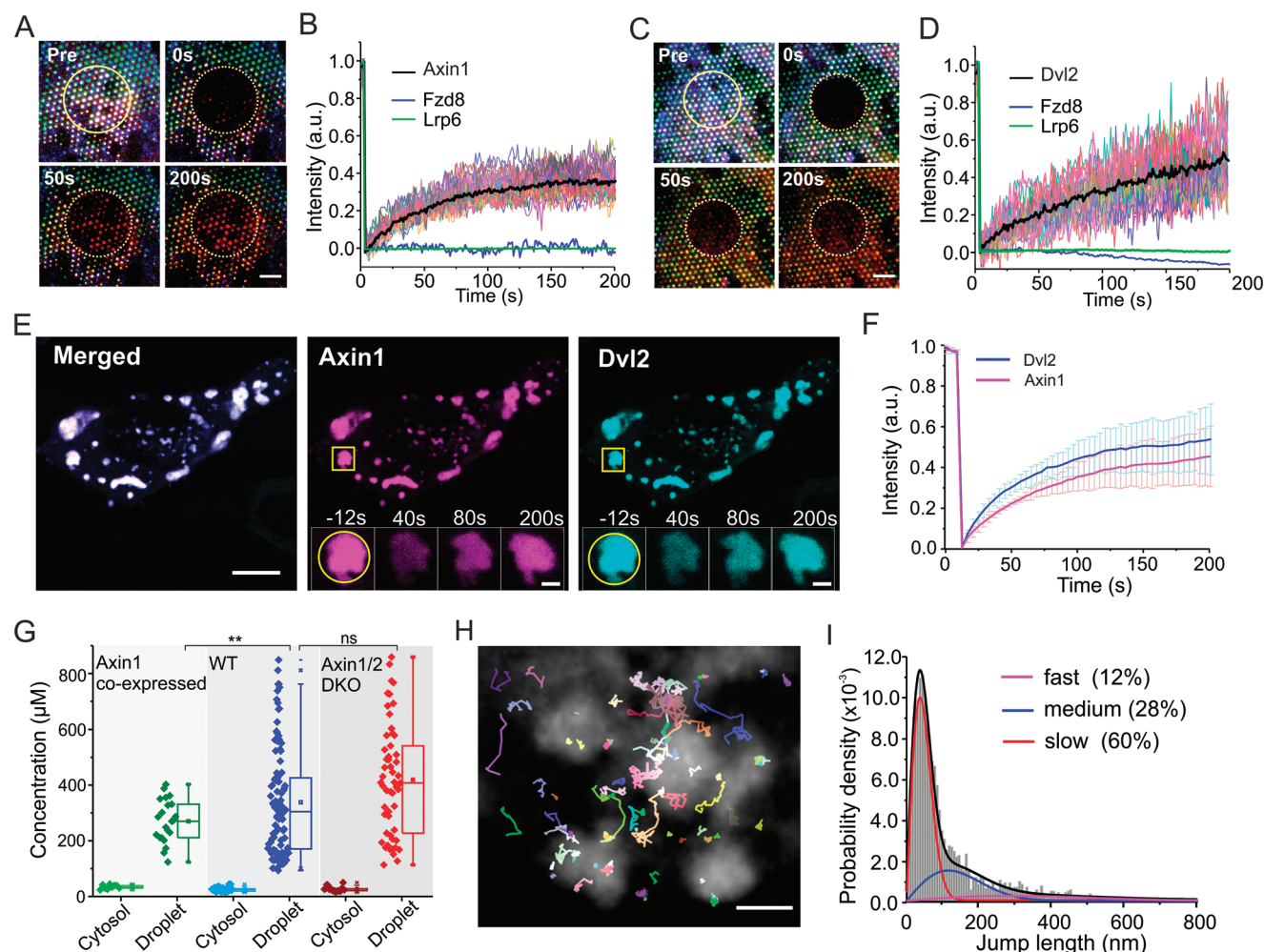


Figure 5. Dynamics of Axin1 and Dvl2 in signalodots and in the cytosol. A,B) Dynamics of Axin1, Fzd8, and Lrp6 co-recruited into Wnt signalodots. A) Representative 3-color time-lapse TIRF images of a HeLa cell co-expressing mEGFP-Lrp6 (green), SNAP-Fzd8 labeled with Dy647 (blue) and tdmCherry-Axin1 (red) after photobleaching within the indicated circular region (cf. Video S1, Supporting Information). Scale bar: 5 μm . B) Average FRAP curves of Lrp6 (green), Fzd8 (blue), and Axin1 (black) from the Wnt signalodots. 30 individual recovery curves of Axin1 bNDAs are shown at background. C,D) Dynamics of tdmCherry-Dvl2, SNAP-Fzd8 and Lrp6 co-recruited into Wnt signalodots. C) Representative 3-color time-lapse TIRF images of a HeLa cell co-expressing mEGFP-Lrp6 (green), SNAP-Fzd8 labeled with Dy647 (blue) and Dvl2-tdmCherry (red) after photobleaching within the indicated circular region (cf. Video S2, Supporting Information). Scale bar: 5 μm . D) Average FRAP curves of Lrp6 (green), Fzd8 (blue) and Dvl2 (black) from the Wnt signalodots. 30 individual recovery curves of Dvl2 bNDAs are shown. E,F) Dynamics of Axin1/Dvl2 co-condensates in the cytosol of living cells. E) Representative confocal microscopy image of HeLa cell overexpressing HaloTag-Axin1 labeled with SiR (magenta) and Dvl2-mCherry (cyan). Inset shows a time-lapse FRAP experiment of a zoomed region (cf. Video S3, Supporting Information). Inset scale bar: 2 μm . F) FRAP curves of Axin1 (magenta) and Dvl2 (blue) obtained from fully bleached droplet (s.d. from triplicate experiments). G) Quantification of the concentrations of Dvl2-mCherry in the cytosol and in the droplet for three types of HeLa cells: WT, wild type. Axin1/2 DKO: Axin1/2 double knockout HeLa cell. H,I) Diffusion of Dvl2 inside Dvl2 droplets resolved by single-molecule tracking. H) Colored trajectories of individual Dvl2-HaloTag labeled with SiR in Dvl2-mCherry droplets shown in the background (gray). Scale bar: 2 μm . I) Step-length histogram analysis of diffusion constants from single-molecule trajectories.

Axin1 and Dvl2 interacting with the co-receptors as depicted in **Figure 6A**.^[38,55,58] To explore this hypothesis, we implemented direct recruitment of Axin1 and/or Dvl2 to the plasma membrane using an intracellular anti-GFP nanobody (GFPnb) fused to an artificial transmembrane helix as depicted in **Figure 6B**. The extracellular terminus of the transmembrane helix was fused to an anti-ALFtag nanobody (ALFAnb) for capturing into bNDAs obtained by stamping BSA conjugated with the ALFtag (ALF^{BSA}). Axin 1/2 double knockout (DKO) HeLa cells co-expressing this bifunctional transmembrane crosslinker ALFAnb-TMD-GFPnb and mEGFP-Axin1 cultured on ALF^{BSA}

bNDAs showed efficient nanopatterning of Axin1 (**Figure 6C**). Strikingly, the Axin1 bNDAs showed characteristic topological features of protein nanodroplet arrays, which were corroborated by DIC and SEM imaging (**Figure 6D**; **Figure S5A–D, I–L**, Supporting Information). Such features were not observed for Lrp6-based signalodots, suggesting different physicochemical properties of the nanodroplets.

As expected, co-expression of Dvl2-tdmCherry yielded recruitment into mEGFP-Axin1 nanodroplet bNDAs (**Figure 6E**), suggesting co-condensation as observed in the cytosol. FRAP experiments, however, revealed that Dvl2, but not Axin1, was

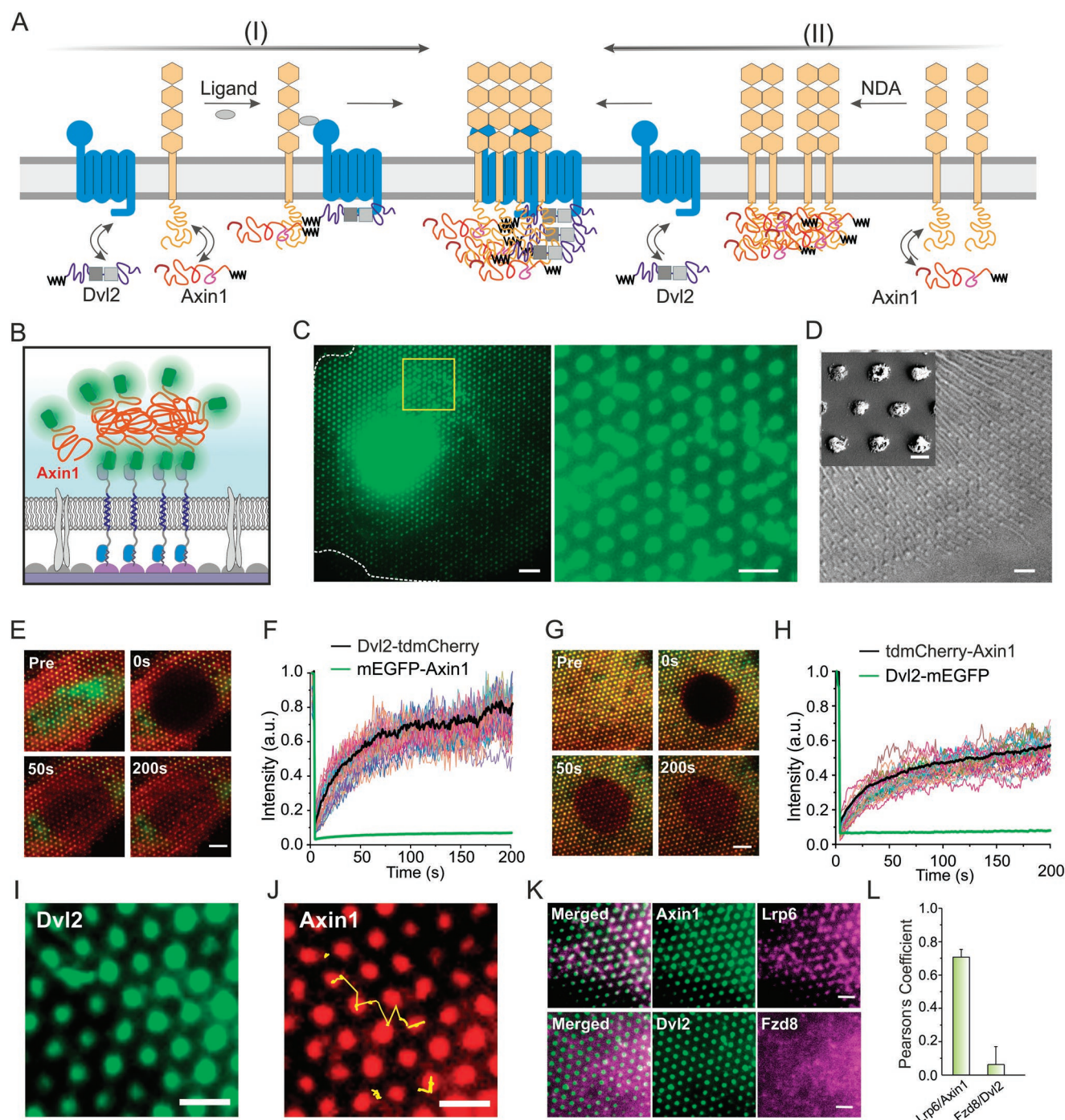


Figure 6. Wnt signalosome assembly driven by Axin1/Dvl2 co-condensation with co-receptors. **A)** Formation of Wnt signalosomes mediated by co-condensation of Axin1 and Dvl2 can be induced by Wnt agonists that heterodimerize Fzd and Lrp6 (I) or by clustering of Lrp6 via bNDA (II). **B)** Cartoon of capturing mEGFP-Axin1 into $ALFA_{BSA}$ bNDAs using an artificial transmembrane crosslinker ALFAnb-TMD-GFPnb. **C)** TIRF imaging of a HeLa cell co-expressing mEGFP-Axin1 and ALFAnb-TMD-GFPnb that were cultured on $ALFA_{BSA}$ bNDAs. Overview (left) and zoom-up (right) of a region highlighted in yellow. Scale bar: 5 μ m (2 μ m in the zoom-up). **D)** Differential interference contrast (DIC) image indicates mEGFP-Axin1 bNDA being nanodroplet arrays. Scale bar: 2 μ m. Inset: Scanning electron microscopy (SEM) of individual mEGFP-Axin1 nanodroplets. Scale bar: 500 nm. **E, F)** Co-condensation of Dvl2 upon capturing mEGFP-Axin1 into bNDA. **E)** Time-lapse dual-color fluorescence imaging. Red: Dvl2-tdmCherry. Green: mEGFP-Axin1. Scale bar: 5 μ m. **F)** FRAP curves obtained from 30 individual nanodroplets. **G, H)** Co-condensation of Axin1 upon capturing Dvl2-mEGFP into bNDA. **G)** Time-lapse dual-color fluorescence imaging. Red: tdmCherry-Axin1. Green: Dvl2-mEGFP. Scale bar: 5 μ m. **H)** FRAP curves of 30 individual nanodroplets. **I)** Dvl2-mEGFP nanodroplets (green). **J)** tdmCherry-Axin1 nanodroplets (red). Scale bars: 2 μ m. Yellow trajectories mark the moving Axin1 droplets. **K)** Receptor recruitment by Axin1 bNDA (top) and Dvl2 (bottom) bNDA. Scale bars: 2 μ m. **L)** Correlation analysis of receptor recruitment into the nanodroplet arrays.

rapidly exchanged in these co-condensates (Figure 6E,F; Figure S6A, Supporting Information). Likewise, capturing of Dvl2-mEGFP into bNDAs via transmembrane crosslinker yielded formation of nanodroplets (Figure S5E–H, Supporting Information) and co-condensation of Axin1 (Figure 6G). FRAP of Axin1 captured into Dvl2 bNDAs showed (56 ± 7.6) % recovery within 200 s ($N = 30$), while negligible exchange was observed for Dvl2 (Figure 6G,H). Of note, FRAP of the artificial co-condensation of either Axin1 or Dvl2 yielded a constantly $\approx 40\%$ higher recovery than that observed in Lrp6 bNDA-based signalodots (cf. Figure 5B,D). These results highlight the different properties of Axin1/Dvl2 co-condensates depending on the subcellular context and the interactions with receptors. These differences lead to a heterogeneous intensity distribution of β -catenin immunofluorescence staining which impeded the quantification of β -catenin level.

Strikingly, we observed recruitment of Lrp6 into the artificial Axin1 bNDAs (Figure 6K,L; Figure S6C,G, Supporting Information), while Dvl2 nanodroplets did not recruit Fzd8 (Figure 6K,L; Figure S6D,H, Supporting Information). These results further supports our hypothesis that membrane-proximal condensation of Axin1 initiated by Lrp6 clustering drives Wnt signalosome formation, in line with the key role of Axin that has been previously identified.^[59] Another unexpected observation of the Axin1/Dvl2 co-condensates is the non-correlated mobility of Dvl2 and Axin1 droplets in bNDAs (Video S7 and Figure S6E,F, Supporting Information). This intriguing observation suggests that two types of Axin1/Dvl2 co-condensates co-exist. The internal heterogeneity could arise from the fact that Axin1 and Dvl2 each has their unique condensation-sensitive regions to form their own droplets^[60,61] while the shared DIX homolog accounts for inducing joint LLPS.^[43] This result points out that hierarchical organization of LLPS occurs as a common phenomenon as observed previously in stress granules.^[62]

3. Discussion

Spatial reorganization of cell surface receptors by micropatterning^[45,63–74] and nanopatterning^[75–85] of ligands and receptors has emerged as a powerful approach to unravel key determinants of collective cell functions such as adhesion, growth, and differentiation as well as cellular signaling. Spatial control of signaling platforms into nanoscale dimensions, which is relevant for numerous signaling pathways, has remained challenging. Here, we have devised capillary nanostamping for fabrication of biofunctional bNDAs with diameters of ≈ 300 nm. Their size is somewhat larger than that obtained by dip/polymer-beam pen lithography,^[86–88] e-beam lithography,^[75–78] and block copolymer micelle nanolithography,^[79–82] but falls in the range of DNA-directed self-assembly of multi-scale patterns.^[73,74,83–85] In contrast to these aforementioned patterning approaches, capillary nanostamping involves the use of stamps penetrated by pore systems, which may act as reservoir of inks containing nanoparticles and macromolecules.^[89] Capillary nanostamping using the mesoporous silica stamps in this work is a robust bench-top patterning method that can be carried out manually under ambient conditions.^[22,23] Moreover, capillary nanostamping can be automatized using standard

instrumentation used for polymer pen lithography and it can be carried out in multi-color mode.^[90] The rapid, robust, and cost-effective fabrication workflow makes capillary nanostamping very suitable for cell biological applications, which require high throughput and relatively large functionalized areas. The achieved dot dimensions within the diffraction limit of light are an ideal compromise for quantitative fluorescence imaging with maximum signal-to-background.

Capturing of cell surface receptors via bNDAs densely coated with a bivalent GFP clamp ensured close proximity of receptor dimers. The DARPIn-based GFP clamp is a highly stable protein,^[53] which—in contrast to anti-GFP nanobodies—reliably maintains structure and function at the substrate surface even during cell culture at 37 °C. In conjunction with high-density, high contrast capillary nanoprinting of BSA conjugates, we achieved robust capturing of proteins in the plasma membrane of live cells into densities of ≈ 10000 molecules μm^{-2} . Such clustering into nanoscale dimensions with high receptor density and dimerization at molecular is highly relevant to closely mimic native signaling platforms. While requiring overexpression of the relevant receptor and effector proteins, bNDAs enable to systematically explore the correlation of receptor density and effector recruitment.

We here particularly focused on the capabilities to employ bNDAs for interrogating and controlling protein condensation at the plasma membrane, which is currently emerging as a fundamental principle responsible for dynamic assembly of signaling platforms.^[16] Using Wnt signalosome as a prominent example, we found that capturing Lrp6 into bNDAs promotes agonist-independent recruitment of the co-receptor Fzd8 and the cytosolic effector proteins Axin1 and Dvl2. Increased β -catenin expression levels confirmed downstream signaling activity of these Wnt signalodot arrays. Highly parallel bNDAs providing different receptor densities at single cell level enabled systematic correlation of interactions and analyzing their dynamics. These studies revealed the key role of Lrp6 density for signalodot assembly with molecular distances (≈ 10 nm) between Lrp6 molecules being required to efficiently initiate recruitment of all three partners. Interestingly, this threshold matches the average distance of Axin1 in co-condensates with Dvl2 we found upon co-overexpression of both proteins in the cytosol. These observations strongly support that Wnt signalosome formation is driven by co-condensation Axin1 and Dvl2 together with the receptors Lrp6 and Fzd8, which in turn is counteracting the destruction complex. Strikingly, bNDA could also be used to directly capture Axin1/Dvl2 co-condensates to the plasma membrane. Distinct morphology and phase behavior corroborate that interactions with the receptors alter the properties of Axin1/Dvl2 co-condensates, which likely is related to its functional switch. These applications highlight the unique capabilities of biofunctional bNDAs to investigate signaling-regulatory condensates at the plasma membrane of live cells, which so far have remained challenging to control.^[91,92]

4. Experimental Section

Materials: Details of all used reagents can be found in the Table S3 (Supporting Information). If not mentioned otherwise, materials were used directly as purchased or received.

Protein Expression, Purification, and Labeling: To generate tandem GFP binders used for surfaces bio-functionalized with HTL, a construct of anti-GFP clamp R7^[53] followed by a (Gly-Ser-Asp)₃ linker, the HaloTag, a second R7 and an octa-HisTag (tdClamp-HaloTag) was cloned into a pET21a vector. The tdClamp-HaloTag protein was produced in *Escherichia coli* BL21 (DE3) Rosetta cells. The cells were grown in the presence of ampicillin to an OD₆₀₀ of 0.6 and induced with 0.5 mM IPTG at 37 °C for 5 h. For purification, cells were resuspended in HBS buffer (20 mM HEPES, pH 7.5, 300 mM NaCl) supplemented with DNase, lysozyme and EDTA-free protease inhibitor mix. After disrupting the cells by sonication and ultracentrifugation, the supernatant was filtered and loaded onto a 5 mL HisTrap HP column (GE Healthcare) for immobilized metal affinity chromatography. The pooled fractions containing tdClamp-HaloTag were purified by size exclusion chromatography on a HighLoad Superdex 200 pg 16/60 column (GE Healthcare). Aliquots from combined fractions were frozen in liquid nitrogen and stored at -80 °C until usage.

mEGFP with an N-terminal hexahistidine tag (mEGFP), mEGFP with an N-hexahistidine tag-HaloTag (HaloTag-mEGFP), and mCherry with an N-terminal hexahistidine tag (mCherry) were cloned in the pET21a plasmid, respectively. The proteins were expressed in *Escherichia coli* BL21 (DE 3) Rosetta cells, followed by purification of immobilized metal affinity chromatography and size exclusion chromatography as previously reported.^[93] The next generation surrogate (NGS) Wnt was produced as reported before.^[34]

Dvl2 flanked with N-terminal mEGFP and C-terminal hexahistidine tag was cloned in the pET21a plasmid and produced in *Escherichia coli* BL21 RIL cells. The cells were grown in the presence of ampicillin and chloramphenicol to an OD₆₀₀ of 0.5. Protein expression was induced with 0.5 mM IPTG at 37 °C overnight. For protein purification, cells were resuspended in a UREA buffer (8 M urea, 20 mM HEPES pH 7.5, 150 mM NaCl). The cells were disrupted by sonication and the cell lysate was subjected to ultracentrifugation. The supernatant was filtered and loaded onto a 5 mL HisTrap HP column (GE Healthcare) equilibrated in UREA buffer. After buffer exchange with HBS followed by gradient elution with HBS containing 1 M imidazole, the fractions were pooled and mixed with 50 mM EDTA and 20 mM DTT for 1 h. The pooled fractions were then loaded onto a Superdex 200 10/300 gel filtration column (GE Healthcare) for size exclusion chromatography in HBS buffer. Aliquots were frozen in liquid nitrogen and stored at -80 °C until usage.

Synthesis of BSA Conjugates: For synthesis of HTL-BSA, a bovine serum albumin solution (1 g in 5 mL HBS buffer) was dialyzed in 2 L HBS buffer for 48 h at 4 °C (14 kDa cutoff). Concentration of the remaining purified BSA was determined by UV-vis spectrometer. 369 µL the dialysis-purified BSA (0.37 µmol) was added to 3.4 mL HBS together with a solution of 96 mg EDC (0.5 mmol) in 1 mL HBS. 1.7 mg HTL-NH₂ (7.6 µmol) in 200 µL ethanol was then added to the reaction mixture and shaken overnight at 4 °C. The reaction mixture was dialyzed in 2 L HBS for 24 h at 4 °C (14 kDa cutoff), resulting in a 62.8 µM HTL-BSA solution. MALDI analysis showed a broad peak at 69334 m/z compared to the unfunctionalized BSA (66294 Da measured by MALDI). The average mass difference of 3081 m/z corresponds to a degree of functionalization 13.6 HTL moieties per BSA molecule.

For synthesis of ALFA-BSA, 4 mg cysteine-containing ALFA peptide (Ac-CPSRLLEELRRRLTE-COOH, 2.0 µmol) was dissolved in 300 µL HBS (pH: 6.5) followed with addition of 1.3 mg Mal-PEG₂-NHS (3.1 µmol). The mixture was shaken for 15 min before adding 259.2 µL of the dialysis purified BSA (0.41 µmol). The solution was gently shaken overnight at 4 °C and dialyzed in HBS for additional 48 h at 4 °C (14 kDa cutoff), resulting in a 151 µM ALFA-BSA solution. MALDI analysis showed convoluted broad peaks at 66932 m/z, 69272 m/z, and 71267 m/z indicating a mixture of un-functionalized BSA, mono- and bi-functionalized ALFA-BSA with an estimated molar ratio of 1:1.2:1.

^{AT647N}BSA was synthesized by mixing the purified BSA (200 µL, 1.5 mM) and ATTO647N-NHS in a 1:1 molar ratio in HBS buffer for 4 h at room temperature. The crude product was purified with an Amicon Ultra (3K) centrifugal filter and the supernatant was used for stamping.

Surface Modification on Glass: Glass substrates and silica transducers for reflectance interference measurements (the RIFs chips) were cleaned

with a lint-free cloth and plasma cleaned for 10 min in a Diener Femto plasma cleaner prior to the silanization. Immediately after cleaning, the substrates were immersed into a 2% v/v silane solution in dry toluene for 1 h. After the given time the substrates were rinsed thoroughly with toluene and ethanol to remove residual unreacted silane and used within a timeframe of 2 h. This procedure was applied for all silanes with the exception of octadecyltrichlorosilane, which was taken out after a reaction time of 10 min to avoid un-controlled polymerization.

Solid Phase Detection by TIRFS-RIF: A home-built set-up for total internal reflection fluorescence spectroscopy (TIRFS) and reflectance interference (RIF) was used as described in detail before.^[49,94] Surface-sensitive detection of protein binding kinetics were determined in the TIRFS-RIF setup under flow conditions. For TIRFS-RIF detection of HTL-BSA on an NMMS surface in the RIF channel and the TIRF channel, 10 µM HTL-BSA in HBS buffer (20 mM HEPES pH 7.5, 150 mM NaCl) was injected into the flow chamber. Binding of HaloTag-mEGFP to HTL-BSA-covered NMMS surfaces was measured by injecting 2 µM of HaloTag-mEGFP and tagless-mEGFP (negative control) separately into the system. Mass signals and fluorescence signals were recorded simultaneously in RIF channel and TIRFS channel, respectively, which were used for binding kinetic analysis of protein binding (BIAevaluation 3.0 software).

Capillary Nanostamping: Mesoporous silica stamps were prepared following procedures described by Schmidt et al.^[23] Water-soaked stamps were washed by placing them in ethanol for ≈1 day and refreshing the ethanol at least three times. The ethanol-soaked stamps were immersed into MilliQ water which was repeatedly refreshed until the solvent was exchanged. Then the stamps were infiltrated for ≈30 min with 15 µM HTL-BSA or ALFA-BSA in HBS. In order to remove the excess ink, the stamp was dried under a stream of nitrogen until a clear rainbow shine was visible. After attachment to the stamp holder via double-sided tape, the NMMS-modified glass substrates were subjected to patterning for ≈3–5 s and backfilled with 100% fetal bovine serum (FBS). For multiple patterning cycles, new inks were added on the structured stamp surface for ≈1 min and blown dry afterward. Stamping with fluorescently labeled BSA was performed by using 1.6 µM ^{AT647N}BSA in HBS as ink. The patterned samples were backfilled with FBS for 10 min and washed with HBS. The patterned slides were washed with water and stored in PBS until further use.

Cell Culture, Transfection, and Immunofluorescence: HeLa cells (DSMZ no.: ACC57, German Collection of Microorganisms and Cell Cultures) were cultivated at 37 °C, 5% CO₂ in Dulbecco's Modified Eagle's Medium supplemented with 10% FBS. Axin1/2 DKO HeLa cell line was generated by Cyagen US Inc. via CRISPR/Cas9 gene knockout (Contract No. SCS181212J1M1). The gRNAs used for Axin1 are: 1) AGACTTCGACGCCCACTCCGAGG and 2) TCCAGTAGACGGTACAGCGAAGG. gRNAs for Axin2 are: 1) ACACAGCGCGGAACGAAGATGGG and 2) GTGCAAACTTTCGCCCACTCCGAGG. A homozygous clone was selected out. Double knock-out of Axin1 and Axin2 in the homozygous clone was validated by RT-PCR (Axin1: FW-primer: CTCTGGTCTGTTCATGGACC. BW-primer: CCTGAAACGTCCACTCTCTCC; Axin2: FW-primer: GCCGATTGCTGAGAGGAAT. BW-primer: AGTCAGCACTGGAAGACTGC) and DNA sequencing. The results showed genetical deletions of 756 bp for Axin1 and 563 bp for Axin2 at Exon 2, respectively. Due to the deletions, the residual Axin1 contains 58 aa of the original N-terminal Axin1 and stops at 114 aa (hAxin1 full length 862 aa). The residual Axin2 contains 58 aa of the N-terminal and stops at 79 aa (hAxin2 full length 843 aa).

Transient transfection was carried out by a polyethyleneimine (PEI) transfection protocol. Details of protein plasmids can be found in Table S2 (Supporting Information). Briefly, HeLa cells were plated onto a 6 cm Petri dish and grown overnight. 5 µg of each plasmid was added to 300 µL 150 mM NaCl, then vortexed and mixed with 10 µL PEI. After 15 min incubation at room temperature, the mixture was transferred to the seeded HeLa cells for 2–3 h, followed with twice PBS washing and kept in the incubator overnight. For experiments of artificial LLPs, transfections of HaloTag-Axin1 and Dvl2-tdmCherry were performed

according to Viafact protocol (Promega) with a ratio of 1 µg DNA to 3 µl Viafact reagent and kept overnight in incubator. The transfected HeLa cells were detached from the petri dish by Trypsin/EDTA treatment and seeded on a prepared coverslip. After incubation of 6–15 h, the samples were used for microscopy imaging. For labeling of Fzd8-SNAP on bNDA, 100 nM SNAP-Surface 549 or SNAP-Surface 647 was added to the cell culture medium for 30 min at 37 °C. Labeling of HaloTag was conducted by adding 50 nM SiR-HTL for 20 min at 37 °C. For single-molecule tracking experiment, 500 pM SiR-HTL was used for sub-stoichiometric labeling of HaloTag-Dvl2. After labeling, the cells were washed three times with PBS and then immersed in cell culture medium for microscopy imaging experiments.

For immunostaining, cells were fixed with 1 mL 4% PFA in HBS for 15 min at RT. Afterward, the fixation mixture was slowly siphoned off and the glasses were washed with PBS three times for 5 min each. The fixed cells were subjected to 0.1% v/v solution of Triton-X100 in PBS for 10 min, washed three times with PBS, and blocked with a solution of 3% m/m BSA in PBS for 30 min. After removing the blocking solution, 20 µL of a 1:1000 diluted antibody solution with 3% BSA was added to the coverslips and topped off with a small piece of parafilm. The sample was placed in a loosely closed container and put into the 4 °C fridge overnight. The samples were washed three times again with PBS and placed into a microscopy sample holder for fluorescence imaging.

Total Internal Reflection Fluorescence Microscopy (TIRFM): TIRF imaging was carried out at 25 °C using an inverted microscope (Olympus IX-83) with two decks equipped with a 4-Line TIRF condenser (cellTIRF (MITICO), Olympus) in the upper deck and a cellFRAP module (Olympus) in the lower deck. The setup was equipped with a 405 nm laser (BCL-100-405, CrystaLaser), 488 nm diode laser (LuxX 488-200, Omicron), as well as a 561 nm (2RU-VFL-P-500-561-B1R, MPB Communications) and 642 nm fiber laser (2RU-VFL-P-500-642-B1R, MPB Communications). Fluorescence excitation and detection was accomplished by using a TIRF pentaband polychroic beamsplitter (Semrock zt405/488/561/640/730rpc) and a penta-bandpass emitter filter (BrightLine HC 440/521/607/694/809). Emission was further filtered by single bandpass filters used for each channel (blue: Semrock BrightLine HC 445/45, green: Semrock BrightLine HC 525/35, orange: Chroma 600/50 ET, red: Chroma 685/50). Images were acquired with an electron-multiplying CCD camera (Andor iXon Ultra 897) using either a 150× oil immersion objective (Olympus UAPON 150× TIRF, NA 1.45) or a 100× oil immersion objective (Olympus UPLAPO 100× HR, NA 1.5) with and without an additional 1.6× magnification (IX3-CAS, Olympus). Differential interference contrast (DIC) images were taken with the standard DIC condenser of the microscope. The software for imaging was CellSens Dimension (Version 3.1, Olympus).

For fluorescence recovery after photobleaching (FRAP) on bNDAs, the Olympus cellFRAP module was used in combination with a 405 nm bleaching laser (LuxX+ 405–60, Omicron). Images were acquired with a 3-Line polychroic beamsplitter (Chroma, zt488/561/633,405tpc) in the upper deck combined with a FRAP cube in the lower deck consisting of a dichroic beamsplitter at 405 nm (Chroma, H 405 LPXR superflat) with a QuadLine emitter filter (Chroma, zet405/488/561/640m). Three pre-bleaching images were recorded for a circular region of interest (ROI) with ≈20 µm diameters at full laser power. Images were acquired at the time interval of one frame per second for 4 min. Within the bleached area, individual nanodots ($N = 20\text{--}40$) were selected and the fluorescence intensity of each was measured separately ($F_{\text{nanodot}}(t)$). The intensities of each nanodot $F(t)$ were corrected against photobleaching using the following equation:

$$F(t) = \frac{F_{\text{nanodot}}(t)}{\left(\frac{F_{\text{ref}}(t)}{F_{\text{ref}}(0)} \right)} \quad (1)$$

with $F_{\text{ref}}(t)$ being the fluorescence of unbleached dots and $F_{\text{ref}}(0)$ the intensity of the same dots before bleaching.

Direct stochastic optical reconstruction microscopy (dSTORM) image sequences were acquired in the presence of 500 µL of a 2-amino-2-(hydroxymethyl)propane-1,3-diol (TRIS) imaging buffer (150 mM TRIS pH 8.5, 10 mM NaCl) containing 2% β-mercaptoethanol, 10 mg mL⁻¹ glucose, 0.04 mg mL⁻¹ catalase, 0.5 mg mL⁻¹ glucose oxidase as an oxygen scavenger system. To achieve stable single-molecule blinking conditions, the sample area was illuminated with the 642 nm laser at full intensity for roughly 2 min to transfer most AT647N to into the dark state. Raw data sets consisted of 30,000 frames acquired at 40 fps with an EM gain of 5 at a pixel size of 160 nm. To enable reactivation from the long-lived dark state, an additional constant low-power UV illumination at 405 nm was used. Sample focus plane was held during acquisition with a piezo z-stage (NanoScanZ, NZ100, Prior Scientific). Raw datasets were further processed with the ImageJ plugin ThunderSTORM.^[95] Parameters for image processing were as follows: Image filtering was done via a wavelet (B-spline) filter with order 3 and scale 2, approximate localization of molecules was conducted via a local maximum estimation with a peak intensity threshold equaling 2 times the standard deviation of the wavelet filter used for signal processing. Sub-pixel localization of molecules was performed with an integrated Gaussian method using a fitting radius of 5 pixels and weighted least squares fit.

Single Molecule Tracking: For single molecule tracking in Dvl2 condensate, HaloTag-Dvl2 and mCherry-Dvl2 were co-expressed in HeLa cells using a pSems vector (Table S2, Supporting Information). Sub-stoichiometric labeling of HaloTag-Dvl2 with 500 pM of SiR-HTL was used. Dual-color TIRF microscopy imaging by 561 and 642 nm excitation was carried out in the above-mentioned Olympus TIRF 4-Line setup. Simultaneously time-lapse imaging of the 561 and 642 channels was acquired with a frame rate of 30 fps. To highlight the Dvl2 condensation, images of the mCherry-Dvl2 channel (561 channel) were Z-projected into an overlapping image using ImageJ software (v1.49i).^[96] Single molecule tracking and the step length histogram analysis of the SiR-labeled HaloTag-Dvl2 was performed as previously reported.^[97,98] A triple-component Gaussian model was found to be the optimal fitting model for quantifying the heterogeneous diffusion of Dvl2 in the condensates.

Confocal Laser Scanning Microscopy (cLSM): cLSM imaging was carried out on a confocal laser-scanning microscope (FluoView 1000, Olympus) equipped with a 60× water-immersion objective (UPLSAPO, NA1.2, Olympus). The microscope was equipped with different filter cubes for the orange (U-MWG2, Olympus) and green channel (Exciter bandpass: 474–491 nm, Semrock BrightLine HC 482/18; Emitter bandpass: 505–545 nm, D525/40; Beam splitter: 488 and 647 nm, HC-DB 488/647). Concentration calibrations curves were obtained by using purified mCherry at different gains. For FRAP experiments in cLSM, a circular ROI was selected (8 µm diameter for whole droplet FRAP and 5 µm for sub-droplet FRAP). Three pre-bleach images were recorded before the ROI was illuminated by 405 nm. A time zero intensity I_0 was recorded from the center of the ROI immediately after photobleaching. Fluorescence recovery was monitored with a 4.05 s time interval. The fluorescence intensity in the ROI was obtained by subtracting the time-zero intensity, i.e., $(I_{\text{ROI}}(t) - I_0)$. A reference region outside the photobleached ROI was processed in the same way to obtain $I_{\text{REF}}(t)$. The ROI intensity was normalized to the reference for each time interval using Equation (2):

$$I(t) = \frac{I_{\text{ROI}}(t) - I_0}{I_{\text{REF}}(t) - I_0} \quad (2)$$

where I_0 is the time-zero intensity after photobleaching, $I_{\text{ROI}}(t)$ is the fluorescence intensity within the ROI, and $I_{\text{REF}}(t)$ is the intensity outside the photobleaching ROI. $I(t)$ is the time-dependent intensity used for plotting the FRAP curve.

Scanning Electron Microscopy: Cells for scanning electron microscopy (SEM) were fixed 1 mL 4% PFA in HBS and 1% glutaraldehyde for 1 h at RT. The samples were washed with PBS buffer three times and transferred into an ethanol solution by slowly increasing the ethanol content. Critical point drying was conducted with a Leica Auto CPD300 with liquid CO₂ at 40 °C and 80 bar. The samples were sputtered with platinum/iridium before imaging with a Zeiss Auriga scanning electron microscope

operated at an accelerating voltage of 3 keV. Both secondary electron detector (SEI) and in-lens detector were used for detection.

Image Evaluation: Immunostaining of β -catenin: For every cell, the nucleus was determined through the DIC image and the contour was transferred to the respective fluorescence image in order to determine the intensity values inside the nucleus. Images were acquired under the same conditions for each set of experiments. The results of each set were referenced against untreated wild type HeLa cells for reliable comparison.

Contrast analysis: Contrast analysis of line profiles was performed based on deconvolved images. Values from a line plot were subtracted either with a background outside a cell, when working *in cellulo*, or with a defective spot in the pattern to minimize the effects of intensity overlapping of two neighbor dots. Box-chart contrast analysis of bNDA in the deconvolved image was obtained using the colocalization algorithm (cf. Colocalization analysis of bNDAs). Box-chart diagrams were gained by plotting the determined contrast of individual nanodots for each channel.

Pearson's Coefficient: For the determination of the Pearson's coefficient, three representative cells of the respective experiment were analyzed. For each cell, 3 line plots were drawn through the whole patterned cell and the intensity values in every fluorescence channel were recorded. Pearson's correlation analysis was performed with the obtained values of the corresponding channels. Data are shown as mean value \pm standard deviation.

Image evaluations were performed with the ImageJ (v1.49i). Origin 9 Pro was used for contrast evaluation and statistical analysis.

Colocalization Analysis of bNDAs: The colocalization script was written in Matlab R2018a containing the following three parts:

1. Image deconvolution: A Tikhonov deconvolution was performed to the raw image by reversing the effect of the point spread function (PSF) and shifting all signal back into the nanodots:

$$I = \text{IFFT} \left(\frac{\text{FFT}(\text{PSF})^* \times \text{FFT}(I_{\text{observed}})}{|\text{FFT}(\text{PSF})|^2 + \gamma} \right) \quad (3)$$

Here, PSF = 1.3 pixel was used for blue, 1.4 pixel for green, 1.8 pixel for red. PSF of the microscope was approximated by 2D-Gaussian. $\gamma = 10^{-1.5}$ was used as the regularization factor for smoothness during the deconvolution to suppress the noise enhancement.

2. Nanodot identification: Individual nanodots were identified by smoothing the deconvolved image and then seeking the local maxima in the pixel intensities. In order to discriminate signal against noise, a minimum signal threshold is estimated using Otsu's method.^[99] The detected nanodots were further refined by first calculating the median distance between nanodots and then discarding all nanodots that do not satisfy at least 3 such neighbors ($<1.3 \times$ median distance). The accepted pixels were then thickened radially by 2 pixels (pixel size 130 nm) to capture the whole printed area. Of note, the thickening was done in a way that there is always 1 pixel separating between individual nanodots. Additionally, a cell mask was generated by dilating the image further with 2 pixels or by filling holes if necessary.
3. Contrast calculation and classification: The contrast was calculated by comparing the intensity within a nanodot to the local background determined from the surrounding pixels. After smoothing by lateral interpolation, the average intensities in the individual nanodots and the background were calculated. The contrast was then obtained as the ratio of intensity in the nanodot divided by the background for all channels. Contrast classification was carried out to determine the minimum contrast of Lrp6 (i.e., the threshold) that induces co-recruitment of Fzd8, Axin1 and/or Dvl2. To do so, nanodot contrasts of each channel were analyzed by fitting a 2-Fraction Gaussian Mixture against the contrasts obtained in the Lrp6

channel. By setting a minimum value (here using a contrast of 2), we determined the posterior probabilities that belong to the effective response fraction (marked in red in the figures). The minimum value was then sampled via bootstrapping the 5% percentile of the Lrp6 contrast that is responsible for recruitment of proteins in the other two channels. The minimum contrast of Lrp6 was determined when the responses being close to $\log(\text{ratio}) = 0$ by checking the contrast distributions of other channels. To this end, the power law dependencies as well as a correlation coefficient were determined together with the minimum contrast of Lrp6.

Statistical Analysis: Data were presented as mean \pm SD. For immunofluorescence staining of β -catenin, $n > 15$ cells. For Pearson's correlation analysis, $n = 3$ cells with three lines each. For single nanodot intensity analysis, $n \geq 700$. For FRAP analysis, $n \geq 25$. The Student's t-test was used to compare the means between two independent sample groups. Statistical significance was defined by p -values of $*p \leq 0.05$, $**p \leq 0.01$, and $***p \leq 0.001$. Image evaluations were performed with the ImageJ (v1.49i). Origin 9 Pro was used for contrast evaluation and statistical analysis. Single nanodot intensity analyses were performed with Matlab R2018a.

Supporting Information

Supporting Information is available from the Wiley Online Library or from the author.

Acknowledgements

The authors thank H. Kenneweg, A. Budke-Gieseking, G. Hikade, and W. Kohl for the excellent technical assistance. This project was supported by funding to C.Y., J.P., and R.K. from the DFG (YO 166/1-1, SFB 944, projects P8 and Z, and the DFG Facility iBiOs, PI 405/14-1), funding to M.S. from the European Research Council (ERC-CoG-2014, Project 646742 INCANA) and by intramural funding to M.S., J.P. and C.Y. from Osnabrück University within the profile line "Integrated Science".

Open access funding enabled and organized by Projekt DEAL.

Conflict of Interest

The authors declare no conflict of interest.

Authors Contribution

C.Y. and J.P. conceived the project together with M.S. and M.P. M.P. designed and conducted the bNDA experiments and performed the data analysis. M.K. performed the cytosolic LLPS experiments and analyzed the results. C.P.R. conceived and programmed the evaluation software for image analysis. A.P. contributed the GFP trap technology. I.W. performed the protein engineering and characterizing the binding kinetics. S.K. contributed to the synthesis of surface coating materials under the supervision of J.C.M.H. L.J. performed the surface sensitive detection. Y.M. produced the Wnt agonist under the supervision of K.C.G. M.H. and R.K. contributed to superresolution imaging and image evaluations. C.Y. and J.P. wrote the manuscript with contributions from M.S., M.P., and all authors.

Data Availability Statement

The data that support the findings of this study are openly available in bioRxiv at <https://doi.org/10.1101/2022.06.11.495600>, reference number 495600.

Keywords

capillary nanostamping, liquid–liquid phase separation, plasma membrane compartmentalization, protein nanoarrays, signaling platforms, Wnt/ β -catenin signaling

Received: June 15, 2022
Revised: August 30, 2022
Published online:

- [1] A. Kusumi, Y. M. Shirai, I. Koyama-Honda, K. G. N. Suzuki, T. K. Fujiwara, *FEBS Lett.* **2010**, 584, 1814.
- [2] Y. Jaillais, T. Ott, *Plant Physiol.* **2020**, 182, 1682.
- [3] D. Marguet, P.-F. Lenne, H. Rigneault, H.-T. He, *EMBO J.* **2006**, 25, 3446.
- [4] J. Bernardino de la Serna, G. J. Schutz, C. Eggeling, M. Cebecauer, *Front Cell Dev Biol* **2016**, 4, 106.
- [5] S. M. Lu, G. D. Fairn, *Crit. Rev. Biochem. Mol. Biol.* **2018**, 53, 192.
- [6] S. T. Low-Nam, K. A. Lidke, P. J. Cutler, R. C. Roovers, P. M. P. Van Bergen En Henegouwen, B. S. Wilson, D. S. Lidke, *Nat. Struct. Mol. Biol.* **2011**, 18, 1244.
- [7] C. You, T. T. Marquez-Lago, C. P. Richter, S. Wilmes, I. Moraga, K. C. Garcia, A. Leier, J. Piehler, *Sci. Adv.* **2016**, 2, e1600452.
- [8] D. Richter, I. Moraga, H. Winkelmann, O. Birkholz, S. Wilmes, M. Schulte, M. Kraich, H. Kenneweg, O. Beutel, P. Selenschik, D. Paterok, M. Gavutis, T. Schmidt, K. C. Garcia, T. D. Müller, J. Piehler, *Nat. Commun.* **2017**, 8, 15976.
- [9] S. A. Freeman, A. Vega, M. Riedl, R. F. Collins, P. P. Ostrowski, E. C. Woods, C. R. Bertozzi, M. I. Tammi, D. S. Lidke, P. Johnson, S. Mayor, K. Jaqaman, S. Grinstein, *Cell* **2018**, 172, 305.
- [10] M. F. Garcia-Parajo, A. Cambi, J. A. Torreno-Pina, N. Thompson, K. Jacobson, *J. Cell Sci.* **2014**, 127, 4995.
- [11] J. Goyette, K. Gaus, *Curr. Opin. Cell Biol.* **2017**, 44, 86.
- [12] Z. Chen, D. Oh, K. H. Biswas, R. Zaidel-Bar, J. T. Groves, *Elife* **2021**, 10, 67379.
- [13] M. L. Dustin, J. T. Groves, *Annu. Rev. Biophys.* **2012**, 41, 543.
- [14] P. Sil, N. Mateos, S. Buschow, S. Buschow, C. Manzo, K. G. N. Suzuki, T. Fujiwara, A. Kusumi, M. F. Garcia-Parajo, S. Mayor, *Mol. Biol. Cell* **2019**, 31, 18110715.
- [15] W. Y. C. Huang, S. Alvarez, Y. Kondo, Y. K. Lee, J. K. Chung, H. Y. M. Lam, K. H. Biswas, J. Kuriyan, J. T. Groves, *Science* **2019**, 363, 1098.
- [16] L. B. Case, J. A. Ditlev, M. K. Rosen, *Annu. Rev. Biophys.* **2019**, 48, 465.
- [17] S. Banjade, M. K. Rosen, *Elife* **2014**, 3.
- [18] L. B. Case, X. Zhang, J. A. Ditlev, M. K. Rosen, *Science* **2019**, 363, 1093.
- [19] E. W. Martin, T. Mittag, *Science* **2019**, 363, 1036.
- [20] C.-C. Lin, K. M. Suen, P.-A. Jeffrey, L. Wieteska, J. A. Lidster, P. Bao, A. P. Curd, A. Stainthorp, C. Seiler, H. Koss, E. Miska, Z. Ahmed, S. D. Evans, C. Molina-Parás, J. E. Ladbury, *Mol. Cell* **2022**, 82, 1089.
- [21] C.-W. Lin, L. M. Nocka, B. L. Stinger, J. B. Degrandchamp, L. J. N. Lew, S. Alvarez, H. T. Phan, Y. Kondo, J. Kuriyan, J. T. Groves, *Proc. Natl. Acad. Sci. USA* **2022**, 119, 2122531119.
- [22] M. Philippi, C. You, C. P. Richter, M. Schmidt, J. Thien, D. LiäE, J. Wollschläger, J. Piehler, M. Steinhart, *RSC Adv.* **2019**, 9, 24742.
- [23] M. Schmidt, M. Philippi, M. Münzner, J. M. Stangl, R. Wiczorek, W. Harneit, K. Müller-Buschbaum, D. Enke, M. Steinhart, *Adv. Funct. Mater.* **2018**, 28, 1800700.
- [24] J. Bilić, Y.-L. Huang, G. Davidson, T. Zimmermann, C.-M. Cruciati, M. Bienz, C. Niehrs, *Science* **2007**, 316, 1619.
- [25] L. B. Case, J. A. Ditlev, M. K. Rosen, *Annu. Rev. Biophys.* **2019**, 48, 465.
- [26] K. N. Schaefer, M. Peifer, *Dev. Cell* **2019**, 48, 429.
- [27] H. Clevers, K. M. Loh, R. Nusse, *Science* **2014**, 346, 1248012.
- [28] H. F. Farin, I. Jordens, M. H. Mosa, O. Basak, J. Korving, D. V. F. Tauriello, K. De Punder, S. Angers, P. J. Peters, M. M. Maurice, H. Clevers, *Nature* **2016**, 530, 340.
- [29] S. J. Habib, B.-C. Chen, F.-C. Tsai, K. Anastassiadis, T. Meyer, E. Betzig, R. Nusse, *Science* **2013**, 339, 1445.
- [30] B. T. MacDonald, X. He, *Cold Spring Harbor Perspect. Biol.* **2012**, 4, a007880.
- [31] M. Gammons, M. Bienz, *Curr. Opin. Cell Biol.* **2018**, 51, 42.
- [32] C. Y. Janda, L. T. Dang, C. You, J. Chang, W. De Lau, Z. A. Zhong, K. S. Yan, O. Marecic, D. Siepe, X. Li, J. D. Moody, B. O. Williams, H. Clevers, J. Piehler, D. Baker, C. J. Kuo, K. C. Garcia, *Nature* **2017**, 545, 234.
- [33] N. Tsutsumi, S. Mukherjee, D. Waghay, C. Y. Janda, K. M. Jude, Yi Miao, J. S. Burg, N. G. Aduri, A. A. Kossiakoff, C. Gati, K. C. Garcia, *Elife* **2020**, 9, 58464.
- [34] Yi Miao, A. Ha, W. De Lau, K. Yuki, A. J. M. Santos, C. You, M. H. Geurts, J. Puschhof, C. Pleguezuelos-Manzano, W. C. Peng, R. Senlice, C. Piani, J. W. Buikema, O. M. Gbedio, M. Vallon, J. Yuan, S. De Haan, W. Hemrika, K. Rösch, L. T. Dang, D. Baker, M. Ott, P. Depeille, S. M. Wu, J. Drost, R. Nusse, J. P. Roose, J. Piehler, S. F. Boj, C. Y. Janda, et al., *Cell Stem Cell* **2020**, 27, 840.
- [35] Y. Tao, M. Mis, L. Blazer, M. Ustav, Z. Steinhart, R. Chidiac, E. Kubarakos, S. O'Brien, X. Wang, N. Jarvik, N. Patel, J. Adams, J. Moffat, S. Angers, S. S. Sidhu, *Elife* **2019**, 8, 46134.
- [36] H. Chen, C. Lu, B. Ouyang, H. Zhang, Z. Huang, D. Bhatia, S.-J. Lee, D. Shah, A. Sura, W.-C. Yeh, Y. Li, *Cell Chem. Biol.* **2020**, 27, 598.
- [37] A. H. Nile, S. Mukund, K. Stanger, W. Wang, R. N. Hannoush, *Proc. Natl. Acad. Sci. USA* **2017**, 114, 4147.
- [38] K. Tamai, X. Zeng, C. Liu, X. Zhang, Y. Harada, Z. Chang, X. He, *Mol. Cell* **2004**, 13, 149.
- [39] L. J. Bugaj, A. T. Choksi, C. K. Mesuda, R. S. Kane, D. V. Schaffer, *Nat. Meth.* **2013**, 10, 249.
- [40] C. Metcalfe, C. Mendoza-Topaz, J. Mieszczynek, M. Bienz, *J. Cell Sci.* **2010**, 123, 1588.
- [41] L. J. Bugaj, D. P. Spelke, C. K. Mesuda, M. Varedi, R. S. Kane, D. V. Schaffer, *Nat. Commun.* **2015**, 6, 6898.
- [42] T. Schwarz-Romond, C. Metcalfe, M. Bienz, *J. Cell Sci.* **2007**, 120, 2402.
- [43] M. Fiedler, C. Mendoza-Topaz, T. J. Rutherford, J. Mieszczynek, M. Bienz, *Proc. Natl. Acad. Sci. USA* **2011**, 108, 1937.
- [44] W. Kan, M. D. Enos, E. Korkmazhan, S. Muennich, D.-H. Chen, M. V. Gammons, M. Vasishta, M. Bienz, A. R. Dunn, G. Skiniotis, W. I. Weis, *Elife* **2020**, 9, e55015.
- [45] M. Schwarzenbacher, M. Kaltenbrunner, M. Brameshuber, C. Heshe, W. Paster, J. Weghuber, B. Heise, A. Sonnleitner, H. Stockinger, G. J. Schütz, *Nat. Meth.* **2008**, 5, 1053.
- [46] P. Lanzerstorfer, U. Müller, K. Gordiyenko, J. Weghuber, C. M. Niemeyer, *Biomolecules* **2020**, 10, 540.
- [47] G. V. Los, L. P. Encell, M. G. McDougall, D. D. Hartzell, N. Karassina, C. Zimprich, M. G. Wood, R. Learish, R. F. Ohana, M. Urh, D. Simpson, J. Mendez, K. Zimmermann, P. Otto, G. Vidugiris, J. Zhu, A. Darzins, D. H. Klaubert, R. F. Bulleit, K. V. Wood, *ACS Chem. Biol.* **2008**, 3, 373.
- [48] H.-M. Schmitt, A. Brecht, J. Piehler, G. Gauglitz, *Biosens. Bioelectron.* **1997**, 12, 809.
- [49] M. Gavutis, S. Lata, P. Lamken, P. Müller, J. Piehler, *Biophys. J.* **2005**, 88, 4289.
- [50] J. Flesch, M. Kappen, C. Drees, C. You, J. Piehler, *Anal. Bioanal. Chem.* **2020**, 412, 3413.
- [51] J. Piehler, A. Brecht, K. Hehl, G. Gauglitz, *Colloids Surf B Biointerfaces* **1999**, 13, 325.

- [52] D. Liße, V. Wilkens, C. You, K. Busch, J. Piehler, *Angew Chem Int Ed Engl* **2011**, 50, 9352.
- [53] S. Hansen, J. C. Stüber, P. Ernst, A. Koch, D. Bojar, A. Batyuk, A. Plückthun, *Sci. Rep.* **2017**, 7, 16292.
- [54] X. Zeng, K. Tamai, B. Doble, S. Li, H. Huang, R. Habas, H. Okamura, J. Woodgett, X. He, *Nature* **2005**, 438, 873.
- [55] V. S. W. Li, S. S. Ng, P. J. Boersema, T. Y. Low, W. R. Karthaus, J. P. Gerlach, S. Mohammed, A. J. R. Heck, M. M. Maurice, T. Mahmoudi, H. Clevers, *Cell* **2012**, 149, 1245.
- [56] G. Davidson, W. Wu, J. Shen, J. Bilic, U. Fenger, P. Stanek, A. Glinka, C. Niehrs, *Nature* **2005**, 438, 867.
- [57] N. O. Taylor, M.-T. Wei, H. A. Stone, C. P. Brangwynne, *Biophys. J.* **2019**, 117, 1285.
- [58] D. V. F. Tauriello, I. Jordens, K. Kirchner, J. W. Sloodstra, T. Kruitwagen, B. A. M. Bouwman, M. Noutsou, S. G. D. Rüdiger, K. Schwaborn, A. Schambony, M. M. Maurice, *Proc. Natl. Acad. Sci. USA* **2012**, 109, E812.
- [59] X. Zeng, He Huang, K. Tamai, X. Zhang, Y. Harada, C. Yokota, K. Almeida, J. Wang, B. Doble, J. Woodgett, A. Wynshaw-Boris, J.-C. Hsieh, Xi He, *Development* **2008**, 135, 367.
- [60] J. Nong, K. Kang, Q. Shi, X. Zhu, Q. Tao, Ye-G Chen, *J. Cell Biol.* **2021**, 220, 202012112.
- [61] M. V. Gammons, M. Renko, C. M. Johnson, T. J. Rutherford, M. Bienz, *Mol. Cell* **2016**, 64, 92.
- [62] B. Niewidok, M. Igaev, A. Pereira Da Graca, A. Strassner, C. Lenzen, C. P. Richter, J. Piehler, R. Kurre, R. Brandt, *J. Cell Biol.* **2018**, 217, 1303.
- [63] A. J. Torres, M. Wu, D. Holowka, B. Baird, *Annu. Rev. Biophys.* **2008**, 37, 265.
- [64] S. Löchte, S. Waichman, O. Beutel, C. You, J. Piehler, *J. Cell Biol.* **2014**, 207, 407.
- [65] A. Singhai, D. L. Wakefield, K. L. Bryant, S. R. Hammes, D. Holowka, B. Baird, *Biophys. J.* **2014**, 107, 2639.
- [66] G. Arrabito, H. Schroeder, K. Schröder, C. Filips, U. Marggraf, C. Dopp, M. Venkatachalapathy, L. Dehmelt, P. I. H. Bastiaens, A. Neyer, C. M. Niemeyer, *Small* **2014**, 10, 2870.
- [67] E. Sevcsik, M. Brameshuber, M. Fölser, J. Weghuber, A. Honigsmann, G. J. Schütz, *Nat. Commun.* **2015**, 6, 6969.
- [68] C. Dirscherl, R. Palankar, M. Delcea, T. A. Kolesnikova, S. Springer, *Small* **2017**, 13, 1602974.
- [69] D. L. Wakefield, D. Holowka, B. Baird, *Mol. Biol. Cell* **2017**, 28, 3133.
- [70] K. D. Mossman, G. Campi, J. T. Groves, M. L. Dustin, *Science* **2005**, 310, 1191.
- [71] Z. Chen, D. Oh, K. H. Biswas, C.-H. Yu, R. Zaidel-Bar, J. T. Groves, *Proc. Natl. Acad. Sci. U. S. A.* **2018**, 115, 5696.
- [72] M. F. Sánchez, S. Els-Heindl, A. G. Beck-Sickinger, R. Wieneke, R. Tampé, *Science* **2021**, 371, eabb7657.
- [73] R. Garrecht, R. Meyer, J. Duppach, S. Reipschläger, C. Watzl, C. M. Niemeyer, *ChemBioChem* **2016**, 17, 486.
- [74] P. Sun, T. Scharnweber, P. Wadhwani, K. S. Rabe, C. M. Niemeyer, *Small Methods* **2021**, 5, 2001049.
- [75] K. Salaita, P. M. Nair, R. S. Petit, R. M. Neve, D. Das, J. W. Gray, J. T. Groves, *Science* **2010**, 327, 1380.
- [76] H. Cai, J. Muller, D. Depoil, V. Mayya, M. P. Sheetz, M. L. Dustin, S. J. Wind, *Nat. Nanotechnol.* **2018**, 13, 610.
- [77] R. Changede, H. Cai, S. J. Wind, M. P. Sheetz, *Nat. Mater.* **2019**, 18, 1366.
- [78] X. Li, L. H. Klausen, W. Zhang, Z. Jahed, C.-T. Tsai, T. L. Li, B. Cui, *Nano Lett.* **2021**, 21, 8518.
- [79] M. Arnold, V. C. Hirschfeld-Warneken, T. Lohmüller, P. Heil, J. Blümmel, E. A. Cavalcanti-Adam, M. López-García, P. Walther, H. Kessler, B. Geiger, J. P. Spatz, *Nano Lett.* **2008**, 8, 2063.
- [80] X. Wang, S. Li, C. Yan, P. Liu, J. Ding, *Nano Lett.* **2015**, 15, 1457.
- [81] E. H. Schwab, T. L. M. Pohl, T. Haraszi, G. K. Schwaerzer, C. Hiepen, J. P. Spatz, P. Knaus, E. A. Cavalcanti-Adam, *Nano Lett.* **2015**, 15, 1526.
- [82] V. Hortigüela, E. Larrañaga, F. Cutrale, A. Seriola, M. García-Díaz, A. Lagunas, J. Andilla, P. Loza-Alvarez, J. Samitier, S. Ojosnegros, E. Martínez, *Nano Lett.* **2018**, 18, 629.
- [83] A. Shaw, V. Lundin, E. Petrova, F. Fördös, E. Benson, A. Al-Amin, A. Herland, A. Blokzijl, B. Högberg, A. I. Teixeira, *Nat. Methods* **2014**, 11, 841.
- [84] A. Angelin, S. Weigel, R. Garrecht, R. Meyer, J. Bauer, R. K. Kumar, M. Hirtz, C. M. Niemeyer, *Angew. Chem., Int. Ed.* **2015**, 54, 15813.
- [85] T. Verheyen, T. Fang, D. Lindenhof, Y. Wang, K. Akopyan, A. Lindqvist, B. Högberg, A. I. Teixeira, *Nucleic Acids Res.* **2020**, 48, 5777.
- [86] A. Tinazli, J. Piehler, M. Beuttl, R. Guckenberger, R. Tampé, *Nat. Nanotechnol.* **2007**, 2, 220.
- [87] X. Zhang, S. Ding, J. Magoline, A. Ivankin, C. A. Mirkin, *Small* **2022**, 18, 2105998.
- [88] M. D. Cabezas, D. J. Eichelsdoerfer, K. A. Brown, M. Mrksich, C. A. Mirkin, *Methods Cell Biol* **2014**, 119, 261.
- [89] H. Xu, X. Y. Ling, J. Van Bennekorn, X. Duan, M. J. W. Ludden, D. N. Reinhoudt, M. Wessling, R. G. H. Lammertink, J. Huskens, *J. Am. Chem. Soc.* **2009**, 131, 797.
- [90] P. Hou, R. Kumar, B. Oberleiter, R. Kohns, D. Enke, U. Beginn, H. Fuchs, M. Hirtz, M. Steinhart, *Adv. Funct. Mater.* **2020**, 30, 2001531.
- [91] Y. G. Zhao, H. Zhang, *Dev. Cell* **2020**, 55, 30.
- [92] S. Botterbusch, T. Baumgart, *Appl. Sci.* **2021**, 11, 1288.
- [93] T. Wedeking, S. Löchte, C. P. Richter, M. Bhagawati, J. Piehler, C. You, *Nano Lett.* **2015**, 15, 3610.
- [94] S. Lata, M. Gavutis, R. Tampé, J. Piehler, *J. Am. Chem. Soc.* **2006**, 128, 2365.
- [95] M. Ovesný, P. Křížek, J. Borkovec, Z. Švindrych, G. M. Hagen, *Bioinformatics* **2014**, 30, 2389.
- [96] C. A. Schneider, W. S. Rasband, K. W. Eliceiri, *Nat. Methods* **2012**, 9, 671.
- [97] J. Sotolongo Bellón, O. Birkholz, C. P. Richter, F. Eull, H. Kenneweg, S. Wilmes, U. Rothbauer, C. You, M. R. Walter, R. Kurre, J. Piehler, *Cell Rep* **2022**, 2, 100165.
- [98] S. Wilmes, M. Hafer, J. Vuorio, J. A. Tucker, H. Winkelmann, S. Löchte, T. A. Stanly, K. D. Pulgar Prieto, C. Poojari, V. Sharma, C. P. Richter, R. Kurre, S. R. Hubbard, K. C. Garcia, I. Moraga, I. Vattulainen, I. S. Hitchcock, J. Piehler, *Science* **2020**, 367, 643.
- [99] N. Otsu, *IEEE Trans Syst Man Cybern* **1979**, 9, 62.